Quantum Rings in Electromagnetic Fields

A.M. Alexeev and M.E. Portnoi

Abstract This chapter is devoted to optical properties of so-called Aharonov-Bohm quantum rings (quantum rings pierced by a magnetic flux resulting in Aharonov-Bohm oscillations of their electronic spectra) in external electromagnetic fields. It studies two problems. The first problem deals with a single-electron Aharonov-Bohm quantum ring pierced by a magnetic flux and subjected to an in-plane (lateral) electric field. We predict magneto-oscillations of the ring electric dipole moment. These oscillations are accompanied by periodic changes in the selection rules for inter-level optical transitions in the ring allowing control of polarization properties of the associated terahertz radiation. The second problem treats a single-mode microcavity with an embedded Aharonov-Bohm quantum ring which is pierced by a magnetic flux and subjected to a lateral electric field. We show that external electric and magnetic fields provide additional means of control of the emission spectrum of the system. In particular, when the magnetic flux through the quantum ring is equal to a half-integer number of the magnetic flux quanta, a small change in the lateral electric field allows for tuning of the energy levels of the quantum ring into resonance with the microcavity mode, thus providing an efficient way to control the quantum ring-microcavity coupling strength. Emission spectra of the system are discussed for several combinations of the applied magnetic and electric fields.

A.M. Alexeev

School of Physics, University of Exeter, Stocker Road, Exeter EX4 4QL, United Kingdom, e-mail: a.alexeev@exeter.ac.uk

M.E. Portnoi

School of Physics, University of Exeter, Stocker Road, Exeter EX4 4QL, United Kingdom, e-mail: m.e.portnoi@exeter.ac.uk

1 Introduction and overview. Quantum Mechanics in Semiconductor Aharonov-Bohm Quantum Rings and Quantum Electrodynamics in Microcavities.

1.1 Introduction

In their celebrated paper [1] *Aharonov and Bohm* demonstrated that while in classical mechanics the fundamental equations of motion can always be expressed in terms of the field alone, in quantum mechanics a canonical formalism is essential and, as a result, potentials cannot be eliminated from the basic equations. Nanoscale-sized semiconductor rings, which are now commonly called Aharonov-Bohm quantum rings, are among other quantum systems used for experimental studies of the renowned discovery. Few-electron quantum rings with a radial size of $10-20$nm are now easily fabricated. The mean free path of particles confined in these nanostructures exceeds the ring length, which results in the self-interference effects experienced by particles. The influence of the field potentials upon this interference in the regions with vanishing field magnitudes is a direct evidence of the Aharonov-Bohm effect present in quantum rings.

This chapter is devoted to the optical properties of Aharonov-Bohm quantum rings in external electromagnetic fields. The research presented in Section 4 was motivated by a number of works which demonstrated the beneficial influence of an external electric field on some electronic and optical properties of an Aharonov-Bohm quantum ring. The list of these works and a brief description of their main results can be found in Section 1.2. In our work, we study an infinitely-narrow quantum ring subjected to a relatively weak static lateral electric field and pierced by a magnetic flux [2, 3]. We predict magneto-oscillations of the ring electric dipole moment and examine their electric field and temperature dependence. These oscillations are accompanied by periodic changes for the selection rules for inter-level optical transitions in the ring. Radiation associated with these transitions occurs at terahertz frequencies for quantum rings with the radial size of $10-20$nm. Most of the results obtained for the static in-plane electric field can be easily generalized to the case of the rotating field by a proper change of the coordinates system [4].

Exceptional opportunities to control the optical properties of quantum rings with external fields stimulated our further research, which is presented in Section 5. In this work, we study an Aharonov-Bohm quantum ring embedded into a single-mode terahertz microcavity [5].

Microcavity quantum electrodynamics is an area which keeps attracting a strong interest of both the condensed matter and quantum optics research communities. One of the reasons of this everlasting interest is the feasibility of utilizing novel effects originating from field-matter coupling for developing novel nanodevices such as terahertz polariton-lasers. In our studies, we calculate the emission spectrum of the coupled quantum ring-microcavity system and show how it can be tuned by variation of the magnetic field piercing the quantum ring and the lateral electric field. Such control of the emission spectrum was never possible with quantum dots in mi-

crocavities. Advantages arising of using quantum rings instead of quantum dots as photon emitters in microcavities are discussed in Section 5.3 and in Section 6.

The rest of this chapter is organized as follows. In Section 1.2 and Section 2 we provide a cursory overview of quantum phenomena in quantum rings and optical microcavities. In Section 3 some theoretical basics needed for understanding of the later presented research are introduced. Section 4 and Section 5 contain original work as described above. Conclusions and possible extension of this work are included in Section 6.

1.2 Quantum mechanics in nanoscale Aharonov-Bohm quantum rings

Progress in epitaxial techniques in recent decades has resulted in burgeoning developments in the physics of quantum dots (QDs), i.e., semiconductor-based 'artificial atoms'. More recently, a lot of attention has been turned towards non-simply-connected nanostructures, such as quantum rings (QRs), which have been obtained in various semiconductor systems [6, 7, 8, 9, 10, 11, 12, 13, 14, 15, 16, 17, 18, 19, 20, 21, 22, 23, 24, 25, 26, 27, 28, 29, 30, 31, 32]. Originally, QRs were fabricated accidently, when optimizing growth conditions for self-assembled InAs quantum dots on a GaAs substrate, the QD material was splashed out from the QD centre, forming a volcano-like structure [6, 7, 8, 9]. Improved and perfected, it has now become a routine procedure for the fabrication of QRs with typical radii of $10 - 100$nm [11, 12, 13, 14, 16, 18, 19, 21, 22, 23, 24, 25, 26, 27, 28, 29, 30]. In the literature, QRs produced as described above are usually referred to as 'type-I quantum rings'.

Nanostructures with an alternative realization of the ring-shape confinement, the so-called 'type-II quantum dots', were suggested for exploring effects arising from the non-simply-connectedness of such objects. In these nano-sized structures one carrier is confined inside the QD and a carrier of an opposite charge is confined in the barrier [10]. As a result, the carrier in the barrier experiences a rotational movement with a radius of $10 - 20$nm around the QD [15, 33, 20, 31, 32].

Another possible way of QRs fabrication is based on using the evaporative templating method [17]. This fabrication procedure includes three stages: introduction of an aqueous solution which contains QDs and polystyrene microspheres onto the surface of a glass substrate, evaporation, and microsphere removal. During the evaporation stage, QDs surround the microspheres and merge, which finally results in the formation of a QR with the radial dimension of 80nm $- 1\mu$m.

The fascination in QRs is caused by a wide variety of purely quantum mechanical effects, which are observed in ring-like nanostructures (for a review see Refs. [34, 35, 36, 37, 38]). The star amongst them is the Aharonov-Bohm effect, in which a charged particle [1, 39] is affected by a magnetic field away from the particle's trajectory, resulting in magnetic-flux-dependent oscillations of the ring-confined particle energy. The same research group which discovered type-I QRs

was the first to observe the Aharonov-Bohm type oscillations in these nanostructures [9]. This became the starting point for a series of experiments dedicated to the Aharonov-Bohm effect in both type-I QRs [9, 19] and type-II QDs [10, 18, 20, 40].

There is significant interest in the excitonic Aharonov-Bohm effect in QRs, which, in principle, should not exist as the exciton is a neutral particle and can not be influenced by the magnetic field. However, due to the finite size of the exciton, the excitonic Aharonov-Bohm effect is, in fact, possible. The excitonic Aharonov-Bohm effect was theoretically studied by a number of authors in both 1D QRs [41, 42, 43, 44, 45, 46] and 2D QRs [47, 48, 49, 50, 51, 52, 53, 54, 55, 33, 56]. It was shown that the Aharonov-Bohm type oscillations do exist in both 1D and 2D models, but vanish in QRs with the ring radial size larger than the exciton Bohr radius or with increased ring width. Recently, it was demonstrated that in the 2D exactly solvable model previously used in Refs. [57, 58, 59] the magneto-oscillations in the exciton ground state survive down to regimes with radius-width ratio less than unity [60].

To reveal the excitonic Aharonov-Bohm effect it was suggested to place the QR in an external electric field, which delocalizes the relative electron-hole motion around the entire ring [61, 62, 18, 63]. It was also shown that in the presence of an in-plane (lateral) electric field exceeding a particular threshold it is possible to switch the ground state of the QR exciton from being optically active (bright) to optically inactive (dark) [62, 18].

2 Quantum electrodynamics in microcavities: light-matter coupling

The strong coupling regime requires a microcavity (MC) to sustain an isolated mode. Otherwise, the excited mode exponentially decays into the other MC modes. There are three main designs which achieve the goal of zero-dimensional radiation confinement, described below.

The first design, pillar MCs, are fabricated by etching a stack of conventional Bragg mirrors. The typical height of pillar MCs is about 10μm. The lateral confinement in pillar MCs is provided by the reflecting interface between the MC walls and the surrounding media. The chances that the chosen pillar MC contains an emitter (usually, a QD) which is in the strong coupling regime with the MC mode are comparably small and one has to check all produced MCs one by one until a cavity with required characteristics is found.

Another possible realization of a single-mode MC is the photonic crystal cavity. The original idea of a photonic crystal was developed by Yablonovich [64] and John [65]. It is based on the same phenomena which leads to the appearance of bandgaps in semiconductors. A structure with periodic modulations of permittivity becomes forbidden for several ranges of wavelength due to the destructive interferences similar to those of Bragg physics. The first 3D photonic crystal was created by drilling holes in a slab at three different angles, resulting in a full bandgap in

the microwave range [66]. Several years later, a 2D photonic crystal with a bandgap in the optical spectrum was reported [67]. By introducing a defect in the photonic crystal periodic structure it is possible to create a MC (the so-called 'Noda cavity') - radiation becomes trapped within the defect region [68]. Originally, values of the Q-factor in photonic crystal MC were quite small (only around 400), but now using some cunning designs of the photonic crystals periodic structure, MC with Q-factors as large as 10^6 can be fabricated [69]. Some MC designs which promise Q-factors up to 10^9 were also suggested [70].

The last design, the microdisk MC, confines radiation in whispering gallery modes. For a review of microdisk cavities one can refer to Ref. [71].

One of phenomena which can be observed in semiconductor MCs in the Purcell effect [72] in which the time of spontaneous emission is affected by the environment of an emitter. The ratio of the times of spontaneous emission when the emitter is placed in two different environments (e.g., MC and vacuum) is usually referred as the Purcell factor. The first observation of the Purcell effect in semiconductor MCs was done with a QD embedded into a pillar MC [73]. In this experiment, the time of photon spontaneous emission was affected with a Purcell factor of 5. Several similar observations in different systems (e.g., Refs. [74, 75] in pillar MCs, Ref. [76] in microdisk MC, Ref. [77] in photonic crystal MC) followed this pioneering work. For instance, in the experiment of Ref. [77] when a QD was placed inside a photonic bandgap of a semiconductor the time of its spontaneous emission was extended to 2.52ns comparing to the time of 0.65ns when the same QD was placed in the bulk semiconductor. The time of spontaneous emission of another QD placed in the same photonic bandgap and brought into the resonance with the cavity was 0.21ns.

There has been an impressive development towards a better quantum coupling with QDs in MC and improved external control. The latest achievements in fabrication techniques now allow one to position QDs inside MCs with spectacular accuracy. In Ref. [78] a photonic crystal MC with a single QD placed exactly at the maximum of the MC field intensity was demonstrated. In photonic crystal MCs one can spectrally match the MC mode emission with the QD emission by artful etching of the photonic crystal periodic structure. However, once the structure is fabricated, adjustment of any system parameters becomes a difficult task.

The strong coupling regime in QDs in semiconductor MCs was first attained in 2004 in two sequential papers, Ref. [79] in a photonic crystal MC and Ref. [80] in a pillar MC. The strong coupling in microdisc MC was reported a year later [81]. Since then, the strong coupling regime in semiconductor MCs was reported by several research groups, but the number of experiments that achieved this regime remains limited. In this cursory overview, we only provide the list of some of these works - please see Refs. [79, 80, 81, 82, 83, 84, 85, 86, 87]. Two of the listed experiments deserve a more detailed discussion.

In the first work, Refs. [84, 85], the authors developed an electronically controlled device which uses the quantum confined Stark effect [88], in which the external electric field shifts the QD exciton discrete states towards lower energies, to tune QDs in resonance with the mode of the photonic crystal MC. This experiment presents a solution with on-chip control of the strong coupling. But still, due to the

weakness of the phenomena, this way of controlling the QR-MC coupling strength remains somewhat limited. In the second work, Ref. [82], the strong coupling regime was observed with a single QD in a photonic crystal MC. In this experiment the antibunching of the Rabi doublet peaks was proved, which is possibly the first real evidence of full field quantization in a coupled QD-MC system.

A system with a genuine strong coupling should noticeably change its behaviour when an additional quantum of excitation is added or removed. In an ideal picture, an emitter embedded in a MC (e.g., QD or QR) can be modelled as a two-level system coupled to the MC mode. Such a system possesses a Hamiltonian with eigenstates, hybrid light-matter states, form the so-called 'Jaynes-Cummings ladder'. The emission measured outside of the MC should mirror the structure of this 'ladder'.

Lastly, we would like to note that to the best of our knowledge there are no experimental works exploring the strong coupling phenomena in QRs embedded into MCs. We hope that our research presented in Section 5 will stimulate experiments in this area.

3 Theoretical background. Quantum Description of Light-Matter Coupling and the Dipole Approximation for Optical Transitions.

3.1 Introduction

This section contains a brief review of the background theory which is used in the rest of this chapter: quantization of the electromagnetic field, the two-level model for a single-photon emitter, the density matrix operator concept, the equations of motion for the density matrix operator, and the electric dipole approximation. More details of this content can be found in various textbooks, such as Refs. [89, 90, 91, 92, 93, 94, 95, 96].

3.2 Light-matter coupling in microcavities: quantum description

3.2.1 Quantization of the electromagnetic field

Field oscillators - harmonic oscillators.

In the Coulomb gauge the vector potential of a sourceless classical electromagnetic field (CEF) satisfies the requirement

$$\mathrm{div}\mathbf{A}\left(\mathbf{r},t\right) = 0, \tag{1}$$

and the homogeneous wave-equation

$$\frac{1}{c^2}\frac{\partial^2 \mathbf{A}(\mathbf{r},t)}{\partial t^2} - \nabla^2 \mathbf{A}(\mathbf{r},t) = 0, \tag{2}$$

where $\mathbf{r}$ is the position vector and t is the time variable. The field scalar potential can be chosen to be identically zero, so that the field is fully defined by the vector potential

$$\mathbf{E}(\mathbf{r},t) = -\frac{\partial}{\partial t}\mathbf{A}(\mathbf{r},t), \tag{3}$$

$$\mathbf{B}(\mathbf{r},t) = \nabla \times \mathbf{A}(\mathbf{r},t). \tag{4}$$

In what follows we consider a MC of a volume V without specifying its exact shape. The quantization procedure, which we introduce later, does not depend on the MC shape and is the same in MCs with various shapes (e.g., Refs [97] in planar MCs, Ref. [98] in a spherical MCs, Ref. [99] in cylindrical MCs). The solution of Eq. (2) can be written in the following form with separated variables

$$\mathbf{A}(\mathbf{r},t) = \sqrt{1/\varepsilon_0}\sum_i Q_i(t)\,\mathbf{U}_i(\mathbf{r}), \tag{5}$$

where $Q_i(t)$ are the field amplitudes, $\mathbf{U}_i(\mathbf{r})$ is the set of field modes, and ε_0 is the vacuum dielectric permittivity. For the present moment, we assume that all field modes are linearly independent and thus can be orthonormalized. We discuss this assumption in more detail later.

Substitution of Eq. (5) into Eq. (3) and Eq. (4) results in the following expressions

$$\mathbf{E}(\mathbf{r},t) = -\sqrt{1/\varepsilon_0}\sum_i \dot{Q}_i(t)\,\mathbf{U}_i(\mathbf{r}), \tag{6}$$

$$\mathbf{B}(\mathbf{r},t) = \sqrt{1/\varepsilon_0}\sum_i Q_i(t)\,\nabla \times \mathbf{U}_i(\mathbf{r}). \tag{7}$$

Now let us return to the wave equation and substitute the chosen vector potential, given by Eq. (5), into Eq. (2) to obtain

$$\frac{1}{c^2}\left[\ddot{Q}_i(t) + \Omega_i^2 Q_i(t)\right]\mathbf{U}_i(\mathbf{r}) - Q_i(t)\left[\nabla^2 \mathbf{U}_i(\mathbf{r}) + \frac{\Omega_i^2}{c^2}\mathbf{U}_i(\mathbf{r})\right] = 0,$$

Here Ω_i are the frequencies of the field modes. Since each of these equations should be satisfied identically at any time moment and for any position in the space, the expressions in square brackets should vanish separately

$$\ddot{Q}_i(t) + \Omega_i^2 Q_i(t) = 0, \tag{8}$$

$$\nabla^2 \mathbf{U}_i(\mathbf{r}) + \frac{\Omega_i^2}{c^2}\mathbf{U}_i(\mathbf{r}) = 0. \tag{9}$$

One can see that the above equations define CEF time (Eq. (8)) and spatial (Eq. (9)) dynamics.

There are two boundary conditions imposed upon the electromagnetic field inside a MC. Namely, the tangential component of the electric field and the normal component of the magnetic field should vanish at the MC walls. Together with Eq. (1) they lead to the following set of restricting conditions

$$\mathbf{U}_i(\mathbf{r})|_{\text{tang}} = 0 \text{ on the MC walls,}$$

$$\text{curl}\mathbf{U}_i(\mathbf{r})|_{\text{norm}} = 0 \text{ on the MC walls,}$$

and

$$\text{div}\mathbf{U}_i(\mathbf{r}) = 0 \text{ in all MC volume.}$$

It can be shown that the first and the third conditions result in the electric field vanishing on the MC walls. That, in turn, gives $\mathbf{U}_i(\mathbf{r})|_{\text{walls}} = 0$.

Once the exact MC shape is given, using the above conditions, one can solve Eq. (9). The obtained solutions are unique for a given MC. Due to this fact, these solutions are usually called 'normal modes' of the MC. Normal modes fully characterize the geometry of a particular problem.

To be able to proceed with the field quantization we now need to define new functions, the so-called 'normal variables', a_i and a_i^*, which reexpress the field amplitudes Q_i in the following way

$$Q_i = \sqrt{\frac{\hbar}{2\Omega_i}}\left(a_i + a_i^*\right),$$

$$\dot{Q}_i = -i\sqrt{\frac{\hbar\Omega_i}{2}}\left(a_i - a_i^*\right).$$

The expressions above can be inverted. Carrying out this simple operation one obtains the following result

$$a_i = \sqrt{\frac{1}{2\hbar\Omega_i}}\left(\Omega_i Q_i + i\dot{Q}_i\right),$$

$$a_i^* = \sqrt{\frac{1}{2\hbar\Omega_i}}\left(\Omega_i Q_i - i\dot{Q}_i\right).$$

Using the normal variables we can redefine the field vector potential (Eq. (5)) and the electric and magnetic fields (Eqs. (6)-(7)) as

$$\mathbf{A}(\mathbf{r},t) = \sum_i \sqrt{\frac{\hbar}{2\varepsilon_0\Omega_i}}\left(a_i + a_i^*\right)\mathbf{U}_i(\mathbf{r}),$$

$$\mathbf{E}(\mathbf{r},t) = i\sum_i \sqrt{\frac{\hbar\Omega_i}{2\varepsilon_0}}\left(a_i - a_i^*\right)\mathbf{U}_i(\mathbf{r}),$$

$$\mathbf{B}\left(\mathbf{r},t\right) = \sum_i \sqrt{\frac{\hbar}{2\varepsilon_0 \Omega_i}}\left(a_i + a_i^*\right) \mathrm{curl}\,\mathbf{U}_i\left(\mathbf{r}\right).$$

In classical electrodynamics the energy of the electromagnetic field is given by the integral

$$\mathscr{E}_{CEF} = \frac{\varepsilon_0}{2} \int\limits_V \left[\mathbf{E}^2 + c^2\mathbf{B}^2\right] d\mathbf{r}.$$

Performing several transformations it is easy to rewrite this expression in terms of the field amplitudes and the normal variables

$$\mathscr{E}_{CEF} = \frac{1}{2}\sum_i \left[\dot{Q}_i^2 + \Omega_i^2 Q_i^2\right] = \sum_i \hbar\Omega_i a_i^* a_i. \tag{10}$$

Now we need to recall some basics of the quantum harmonic oscillator (QHO). The Hamiltonian of one-dimensional QHO with a unit mass reads as [95]

$$H_{QHO} = \hbar\omega\left(\hat{a}^\dagger\hat{a} + 1/2\right), \tag{11}$$

where ω is the oscillator frequency and $\hat{a}^\dagger$, $\hat{a}$ are the creation and annihilation operators. The eigenstates of the QHO can be denoted by $|n\rangle$ with $n = 0,1,2,..$, so that

$$H_{QHO}|n\rangle = \hbar\omega\left(n + 1/2\right)|n\rangle.$$

These states form the so-called 'QHO ladder'. Each of these states can be constructed from the vacuum state $|0\rangle$, which possesses the property $\hat{a}|0\rangle = 0$, by application of the creation operator n-times:

$$|n\rangle = \frac{\left(\hat{a}^\dagger\right)^n |0\rangle}{\sqrt{n!}}.$$

One can notice that the QHO Hamiltonian given by Eq. (11) is of the same form as the Eq. (10), which defines energy of CEF expressed in terms of normal variables. The only difference is the term $\hbar\omega/2$ which appears due to the non-commutativity of the creation and annihilation operators. Later we show that this term should be omitted in order to normalize energy of the quantized electromagnetic field (QEF) with an infinite number of modes (e.g., QEF in vacuum).

This similarity allows us to proceed with the intuitively simple quantization of the electromagnetic field. The trick is to substitute the normal variables with the creation and annihilation operators, which satisfy the commutation relation $\left[\hat{a}_i, \hat{a}_j^\dagger\right] = \delta_{ij}$ with all other commutators vanishing. The above commutation relation reflects the linear independence of the field modes.

Performing this substitution we arrive at the following expressions for the field vector potential and the electric and magnetic fields

$$\hat{\mathbf{A}} = \sum_i \sqrt{\frac{\hbar}{2\varepsilon_0 \Omega_i}} \left(\hat{a}_i + \hat{a}_i^*\right) \mathbf{U}_i\left(\mathbf{r}\right),$$

$$\hat{\mathbf{E}} = i \sum_i \sqrt{\frac{\hbar \Omega_i}{2\varepsilon_0}} \left(\hat{a}_i - \hat{a}_i^*\right) \mathbf{U}_i\left(\mathbf{r}\right),$$

$$\hat{\mathbf{B}} = \sum_i \sqrt{\frac{\hbar}{2\varepsilon_0 \Omega_i}} \left(\hat{a}_i + \hat{a}_i^*\right) \nabla \times \mathbf{U}_i\left(\mathbf{r}\right).$$

From now on, the electromagnetic field is described with the quantum mechanical operators $\hat{\mathbf{A}}$, $\hat{\mathbf{E}}$, and $\hat{\mathbf{B}}$. Since the creation and annihilation operators entering the equations above do not commute, these operators do not commute as well. One can see that after quantization the time dynamics of the electromagnetic field is hidden in the creation and annihilation operators $\hat{a}_i$ and $\hat{a}_i^\dagger$. Recall that before the quantization procedure the time dependence was defined by the dynamical behaviour of the field amplitudes Q_i.

To finish with the electromagnetic field quantization we should define the Hilbert space of the field eigenstates. We employ once again the analogy with the quantum harmonic oscillator and define the vacuum state of any of the electromagnetic field modes by the requirement $\hat{a}_i |0\rangle = 0$. Due to the independence of field modes we can construct all other eigenstates as a tensor product

$$|n_1, n_2, \ldots, n_k, \ldots\rangle = |n_1\rangle \otimes |n_2\rangle \otimes \cdots \otimes |n_k\rangle \otimes \cdots = \bigotimes_i \frac{\left(\hat{a}_i^\dagger\right)^{n_i}}{\sqrt{n_i!}} |0\rangle,$$

where the index i numbers the field modes and n_i are the non-negative integers usually called 'mode occupation numbers'.

In some cases the number of the field modes in a MC can be infinite and the field energy should be renormalized by omitting the term which is responsible for the vacuum state energy in the field Hamiltonian [89, 90, 91, 92, 93, 94]. In this case the Hamiltonian of the QEF reads

$$H_{QEF} = \sum_i \hbar \Omega_i \hat{a}_i^\dagger \hat{a}_i.$$

In our research presented in this chapter we will consider a MC which sustains just one mode of QEF. In this case the MC field Hamiltonian reads as

$$H_{MC} = \hbar \omega_{MC} \hat{a}^\dagger \hat{a}, \tag{12}$$

where ω_{MC} is the MC mode frequency and we have omitted creation and annihilation operators indices to simplify notation.

Quantization in a cubic box of volume V.

As was discussed above, the set of field modes which is allowed for a particular problem is fully defined by the geometry of a given MC. In this Section we study a MC with a cubic shape. This case is of significant importance as it allows one to introduce the plane wave representation for the QEF.

The most natural set of orthonormal functions in a cubic MC is the set of plane waves given by

$$\mathbf{f}_{\mathbf{k},\alpha} = \frac{\mathbf{e}_{\mathbf{k},\alpha}\exp{(i\mathbf{k}\mathbf{r})}}{\sqrt{V}},$$

where $\mathbf{k}$ is the wave vector and index α represents the wave polarization. The wave vector $\mathbf{k}$ satisfies the dispersion relation $\omega_k = kc$ with $k = |\mathbf{k}|$. This is a consequence of the requirement for the plane wave functions to satisfy the Helmholtz equation. The polarization vectors $\mathbf{e}_{\mathbf{k},\alpha}$ are complex numbers normalized to unity.

The next step is to expand the field vector potential introduced in the previous Section in terms of the cubic MC plane waves

$$\hat{\mathbf{A}} = \sum_{\mathbf{k},\alpha} \sqrt{\frac{\hbar}{2\varepsilon_0 \Omega_k V}} \left[\mathbf{e}_{\mathbf{k},\alpha}\hat{a}_{\mathbf{k},\alpha}\exp{(i\mathbf{k}\mathbf{r})} + \mathbf{e}_{\mathbf{k},\alpha}^*\hat{a}_{\mathbf{k},\alpha}^\dagger\exp{(-i\mathbf{k}\mathbf{r})} \right]. \qquad (13)$$

In the Coulomb gauge, the field vector potential $\hat{\mathbf{A}}$ has only the transverse component. When applied to Eq. (13) this requirement gives

$$\mathbf{e}_{\mathbf{k},\alpha} \cdot \mathbf{k} = \mathbf{e}_{\mathbf{k},\alpha}^* \cdot \mathbf{k} = 0.$$

There are only two linearly independent vectors orthogonal to the wave vector $\mathbf{k}$. We refer to them with the index α, which, for a given $\mathbf{k}$, can now take only two values, $\alpha = 1,2$. Real values of the polarization vector represent two linear polarizations of the electromagnetic field while complex values correspond to two different circular polarizations.

Finally, to finish with the plane wave representation, we reexpress the boundary conditions for the electric and magnetic fields inside a MC in terms of the plane wave functions $\mathbf{f}_{\mathbf{k},\alpha}$.

Using the boundary conditions imposed upon the field modes $\mathbf{U}_i$ in the previous Section we obtain the following periodic boundary conditions for $\mathbf{f}_{\mathbf{k},\alpha}$

$$\mathbf{f}_{\mathbf{k},\alpha}\left(\mathbf{r} + \mathbf{l}_j L\right) = \mathbf{f}_{\mathbf{k},\alpha}\left(\mathbf{r}\right),$$

where L is the length of the MC sides and $\mathbf{l}_j$ is a set of unit vectors directed along the MC edges. From this condition it is easy to retrieve quantization rules for $\mathbf{k}$

$$\mathbf{k} = \frac{2\pi}{L}\left(N_x \mathbf{l}_x + N_y \mathbf{l}_y + N_z \mathbf{l}_z\right),$$

where N_x, N_y, N_z are integer numbers which allow an alternative way to number the MC plane waves. One should not confuse this numbering with the modes occupation numbers introduced earlier.

To conclude this Section we provide expressions for the quantized electromagnetic field operators, the electromagnetic field Hamiltonian, and Hamiltonian eigenstates in the plane wave representation

$$\hat{\mathbf{E}} = i \sum_{\mathbf{k},\alpha} \sqrt{\frac{\hbar \Omega_k}{2\varepsilon_0 V}} \left[\mathbf{e}_{\mathbf{k},\alpha} \hat{a}_{\mathbf{k},\alpha} \exp\left(i\mathbf{kr}\right) - \mathbf{e}^*_{\mathbf{k},\alpha} \hat{a}^\dagger_{\mathbf{k},\alpha} \exp\left(-i\mathbf{kr}\right) \right], \qquad (14)$$

$$\hat{\mathbf{B}} = i \sum_{\mathbf{k},\alpha} \sqrt{\frac{\hbar \Omega_k}{2\varepsilon_0 V}} \left[\left(\mathbf{k} \times \mathbf{e}_{\mathbf{k},\alpha}\right) \hat{a}_{\mathbf{k},\alpha} \exp\left(i\mathbf{kr}\right) - \left(\mathbf{k} \times \mathbf{e}^*_{\mathbf{k},\alpha}\right) \hat{a}^\dagger_{\mathbf{k},\alpha} \exp\left(-i\mathbf{kr}\right) \right], \quad (15)$$

$$H_{QEF} = \sum_{\mathbf{k},\alpha} \hbar \Omega_k \hat{a}^\dagger_{\mathbf{k},\alpha} \hat{a}_{\mathbf{k},\alpha}, \qquad (16)$$

$$|\{n_{\mathbf{k},\alpha}\}\rangle = |\ldots, n_{\mathbf{k}_i,\alpha_i}, \ldots\rangle = \bigotimes_{\mathbf{k},\alpha} \frac{\left(\hat{a}^\dagger_{\mathbf{k},\alpha}\right)^{n_{\mathbf{k},\alpha}}}{\sqrt{n_{\mathbf{k},\alpha}!}} |0\rangle. \qquad (17)$$

From the Eqs. (14)-(16) it is clear that the electric and magnetic field are related by $\hat{\mathbf{B}} = \sum_{\mathbf{k},\alpha} \left(\mathbf{k}/\Omega_k\right) \times \hat{\mathbf{E}}_{\mathbf{k},\alpha}$.

3.2.2 Two-level photon emitter

In Section 3.2.1 we introduced notation in which the QEF is described in the language of QEF modes occupation numbers. In this notation electric and magnetic fields are defined in terms of creation and annihilation operators. In this Section we show how fermionic states of a single-photon emitter (SPE) can be described in the same language.

A single-photon emitter whose excitations obey fermionic statistics can populate only a finite number of eigenstates, with a maximum of one excitation per eigenstate. This restriction is known as the Pauli exclusion principle [95]. Considering such a system in a general way we denote its eigenstates by $|i\rangle$ and the corresponding eigenenergies by ε_i. We assume that this set of eigenstates is orthonormal, $\langle i|j\rangle = \delta_{i,j}$, and complete, $\sum_i |i\rangle \langle i| = 1$. The eigenstate's index i may consist of several quantum numbers.

Instead of the creation and annihilation operators $a^\dagger$ and a, the system can be described with the projector operators

$$\sigma^\dagger_{ij} = |j\rangle \langle i|,$$

and

$$\sigma_{ij} = |i\rangle \langle j|.$$

These projector operators induce promotion from the state i to the state j and from the state j to the state i by creating an excitation in the system in the same way as operators $a^\dagger$ and a create and annihilate an excitation in a particular mode of the QEF. The main difference is that the projector operators can be applied only once as only one excitation is allowed for each of the emitter eigenstates. If $\varepsilon_i < \varepsilon_j$, the projector operator $\sigma_{ij}^\dagger$ acts as the rising operator while the projector operator σ_{ij} acts as the lowering operator, and if $\varepsilon_i > \varepsilon_j$, projector operators swap their roles.

Using this notation a single-photon emitter Hamiltonian can be defined in the following way

$$H_{SPE} = \sum_j \varepsilon_j \ket{j}\bra{j} = \sum_j \varepsilon_j \sigma_{ij}^\dagger \sigma_{ij}. \tag{18}$$

In most practical cases there is only one mode of the QEF which interacts with the single-photon emitter in a MC. This mode is usually tuned to one of the resonances of the emitter and has a relatively narrow spectral bandwidth. If the other eigenstates are separated by energy gaps which are much larger than the energy associated with the MC mode, all eigenstates other than the two which are brought into the resonance can be safely disregarded.

From now on, we assume that the field causes transitions between only two particular eigenstates of the single-photon emitter. We denote these eigenstates by $\ket{g}$ (the ground state) and $\ket{e}$ (the excited state). The energy gap between these two eigenstates we denote by Δ. This approximation to a multi-level quantum emitter we call the 'two-level emitter' (2LE) approximation. It should be noted that such a basic model works exceptionally well for real systems and gives a good insight into the quantum phenomena occurring in realistic experimental systems (e.g., see Refs. [100, 79, 80, 81, 82, 101, 102]).

The Hamiltonian given by Eq. (18) in the 'two-level emitter' approximation reads as

$$H_{2LE} = \Delta \ket{e}\bra{e} = \Delta \sigma^\dagger \sigma, \tag{19}$$

where we chose the zero energy level to coincide with the energy of the ground state $\ket{g}$ and $\sigma^\dagger = \left(\sigma_x + i\sigma_y\right)/2$, $\sigma = \left(\sigma_x - i\sigma_y\right)/2$ with

$$\sigma_x = \begin{pmatrix} 0 & 1 \\ 1 & 0 \end{pmatrix}, \ \sigma_y = \begin{pmatrix} 0 & -i \\ i & 0 \end{pmatrix},$$

being the Pauli matrices acting in the space of the emitter ground $\ket{g}$ and excited $\ket{e}$ states.

3.2.3 Field-emitter coupling

Coupling of the QEF to SPE is the key phenomenon which enters all further considerations. Using the analogy with classical electrodynamics we take the interaction Hamiltonian in the dipole approximation as

$$H_{INT} = -\mathbf{d} \cdot \mathbf{E},$$

where $\mathbf{d}$ is the SPE dipole moment operator and $\mathbf{E}$ is the QEF electric field operator given by Eq. (14) and taken at the position of the SPE. The interaction Hamiltonian can be reexpressed in the following way

$$H_{INT} = -\sum_{\mathbf{k},\alpha} \hat{\mathbf{d}} \cdot \left(\mathbf{E}_{\mathbf{k},\alpha}^{+} + \mathbf{E}_{\mathbf{k},\alpha}^{-} \right), \tag{20}$$

where

$$\mathbf{E}_{\mathbf{k},\alpha}^{+} = i\sqrt{\frac{\hbar \Omega_k}{2\varepsilon_0 V}} \left[\mathbf{e}_{\mathbf{k},\alpha} a_{\mathbf{k},\alpha} \exp\left(i\mathbf{k}\mathbf{r}_{\mathbf{SPE}} \right) \right], \tag{21}$$

and

$$\mathbf{E}_{\mathbf{k},\alpha}^{-} = -i\sqrt{\frac{\hbar \Omega_k}{2\varepsilon_0 V}} \left[\mathbf{e}_{\mathbf{k},\alpha}^{*} a_{\mathbf{k},\alpha}^{\dagger} \exp\left(-i\mathbf{k}\mathbf{r}_{\mathbf{SPE}} \right) \right]. \tag{22}$$

Note that in Eqs. (21)-(22) the field operators $\mathbf{E}_{\mathbf{k},\alpha}^{+}$ and $\mathbf{E}_{\mathbf{k},\alpha}^{-}$ are taken at the position of the SPE. We would like to stress once more that the time dynamics of the QEF is hidden in the creation and annihilation operators. The SPE electric dipole moment operator is given by

$$\mathbf{d} = \sum_{i,j} \mathbf{d}_{ij} |i\rangle \langle j|, \tag{23}$$

where $\mathbf{d}_{ij}$ is the dipole moment operator matrix element calculated between two different states of the SPE

$$\mathbf{d}_{ij} = \langle i| \mathbf{d} |j\rangle = e \int \psi_i^{*}(\mathbf{r}) \, \mathbf{r} \psi_j(\mathbf{r}) \, d\mathbf{r}.$$

In many cases the emitter eigenfunctions possess the property of parity and thus the diagonal matrix elements $\mathbf{d}_{ii} = 0$. Substituting Eq. (23) into Eq. (20) we obtain

$$H_{INT} = -\sum_{\mathbf{k},\alpha} \sum_{i,j} |i\rangle \langle j| \mathbf{d}_{ij} \cdot \left(\mathbf{E}_{\mathbf{k},\alpha}^{+} + \mathbf{E}_{\mathbf{k},\alpha}^{-} \right).$$

In order to show that the above Hamiltonian is Hermitian we open the brackets in the expression above, swap indices $i \leftrightarrow j$ in the second term under summations (since the second summation is over all possible combinations of (i, j) and the case $\mathbf{d}_{ii} = 0$ is allowed), and use the fact that $\mathbf{d}_{ji} = \mathbf{d}_{ij}^{*}$. This results in

$$H_{INT} = -\sum_{\mathbf{k},\alpha} \sum_{i,j} |i\rangle \langle j| \mathbf{d}_{ij} \cdot \mathbf{E}_{\mathbf{k},\alpha}^{+} + |j\rangle \langle i| \mathbf{d}_{ji}^{*} \cdot \mathbf{E}_{\mathbf{k},\alpha}^{-}. \tag{24}$$

From this equation it can be clearly seen that H_{INT} is indeed Hermitian. Let us now transform the interaction Hamiltonian into a form which will be more suitable for further calculations. For the case of 2LE from Eq. (24) we immediately get the following result

$$H_{INT} =$$
$$- \sum_{\mathbf{k},\alpha} \left(|e\rangle \langle g| \, \mathbf{d}_{eg} \cdot \mathbf{E}^+_{\mathbf{k},\alpha} + |g\rangle \langle e| \, \mathbf{d}^*_{ge} \cdot \mathbf{E}^-_{\mathbf{k},\alpha} + |e\rangle \langle g| \, \mathbf{d}^*_{eg} \cdot \mathbf{E}^-_{\mathbf{k},\alpha} + |g\rangle \langle e| \, \mathbf{d}_{ge} \cdot \mathbf{E}^+_{\mathbf{k},\alpha} \right).$$

$$(25)$$

In the expression above there are four terms under summation. We discuss each of them separately:

- The first term corresponds to the transition from the ground state $|g\rangle$ to the excited state $|e\rangle$. As expected, a photon is absorbed as a result of this transition (due to the presence of the anihilation operator in the expression for $\mathbf{E}^+_{\mathbf{k},\alpha}$).
- The second term corresponds to the transition from the excited state $|e\rangle$ to the ground state $|g\rangle$. As expected, a photon is emitted as a result of this transition (due to the presence of the creation operator in the expression for $\mathbf{E}^-_{\mathbf{k},\alpha}$).
- The third term corresponds to the transition from the ground state $|g\rangle$ to the excited state $|e\rangle$. We expect a photon to be absorbed. Contrary to this expectation, the photon is in fact created (due to the presence of the creation operator in the expression for $\mathbf{E}^-_{\mathbf{k},\alpha}$).
- The forth term corresponds to the transition from the excited state $|e\rangle$ to the ground state $|g\rangle$. We expect a photon to be emitted. Contrary to this expectation, the photon is in fact annihilated (due to the presence of the annihilation operator in the expression for $\mathbf{E}^+_{\mathbf{k},\alpha}$).

One can see that the third and forth terms are nonresonant, these terms do not satisfy the energy conservation law. This fact allows one to neglect these terms in the interaction Hamiltonian given by Eq. (24). Another argument which supports this approximation comes from time-dependent perturbation theory. It is well-known that non-resonant transitions have negligibly small probabilities. This approximation is called the 'rotating wave approximation' (the name originates from the form of the interaction Hamiltonian in the reference frame rotating with the frequency of the electromagnetic field) and is widely used in quantum electrodynamics problems [89, 90, 91, 92, 93, 94]. It can be shown that the neglected terms lead to small corrections called Bloch-Siegert shifts [103].

Therefore, the final expression for quantized electromagnetic field - two-level emitter (QEF-2LE) interaction Hamiltonian reads as

$$H_{INT} = - \sum_{\mathbf{k},\alpha} \left(|e\rangle \langle g| \, \mathbf{d}_{eg} \cdot \mathbf{E}^+_{\mathbf{k},\alpha} + |g\rangle \langle e| \, \mathbf{d}^*_{ge} \cdot \mathbf{E}^-_{\mathbf{k},\alpha} \right), \qquad (26)$$

where the electric field operators $\mathbf{E}^+_{\mathbf{k},\alpha}$ and $\mathbf{E}^-_{\mathbf{k},\alpha}$ are given by Eqs.(21)-(22) from the previous Section.

3.2.4 Density matrix operator

The most general way to describe a system, whether it is isolated from the external environment or interacts with it, is based on utilizing the density matrix operator. In what follows we first introduce the basic concept of the density matrix operator and then show how using the master equation approach it is possible to calculate a stationary density matrix of a system in the presence of incoherent pumping and dissipation processes.

Let us consider an ensemble of N identical emitters in quantum states denoted by i and with corresponding wave functions Ψ^i. An average value of an observable O can be calculated for each of these emitters using corresponding operator $\hat{O}$. The statistic average over the whole ensemble is given by

$$\overline{\langle O \rangle} = \frac{\sum\limits_{i=1}^{N} \langle \Psi^i | \hat{O} | \Psi^i \rangle}{N}. \tag{27}$$

The equation above contains two types of averaging - the quantum mechanical averaging, which is given by the matrix element, and statistical averaging, which is given by the sum of the observable value over the ensemble elements divided by the number of elements.

As all emitters in the ensemble are identical, each of them possess the same set of eigenstates φ_n. Thus, the total emitter's states Ψ^i can be expanded in terms of the emitter's eigenstates φ_n as follows

$$\left| \Psi^i \right\rangle = \sum_n C_n^i \left| \varphi_n \right\rangle, \tag{28}$$

where $C_n^i = \langle \varphi_n | \psi^i \rangle$ and $\sum\limits_n |C_n^i|^2 = 1$. Substituting Eq. (28) into Eq. (27) one obtains

$$\overline{\langle O \rangle} = \sum_{m,n} \left(\frac{\sum_{i=1}^{N} C_n^{i\,*} C_m^i}{N} \right) O_{nm} = \sum_{m,n} \rho_{nm} O_{nm}, \tag{29}$$

where we have introduced a new important entity, the density matrix ρ_{nm}, which is given by

$$\rho_{nm} = \sum_{i=1}^{N} C_n^{i\,*} C_m^i / N = \overline{C_n^{i\,*} C_m^i}. \tag{30}$$

The density matrix contains all statistical information about the considered ensemble of emitters. It is easy to show that the density matrix is normalized

$$\mathrm{Tr}\{\hat{\rho}\} = \sum_n \rho_{nn} = \sum_{i=1}^{N} \sum_n C_n^{i\,*} C_n^i / N = \sum_{i=1}^{N} 1/N = 1.$$

Using the matrix multiplication rule Eq. (29) can be written in a shorter and more convenient form

$$\overline{\langle O \rangle} = \sum_{m,n} \rho_{mn} O_{nm} = \sum_n \left(\hat{\rho} \hat{O} \right)_{nn} = \text{Tr}\{\hat{\rho}\hat{O}\}. \tag{31}$$

For instance, for the identity operator $\hat{1}$ using Eq. (31) one straightforwardly obtains

$$\overline{\langle 1 \rangle} = \sum_{n,m} \rho_{mn} \langle \varphi_n | \hat{1} | \varphi_m \rangle = \sum_{n,m} \rho_{mn} \delta_{nm} = \text{Tr}\{\hat{\rho}\} = 1.$$

The representation of the density matrix operator in terms of expansion coefficients C_n^i is only one of many possible expansions. One can see that the final expression for the average value of an observable O is given by the trace of the density matrix operator. The trace of an operator is independent of the basis chosen in the Hilbert space. That means that the density matrix operator can be defined in a more general way. However, it is convenient to try to define the density matrix operator in terms of system eigenstates, but independently of any basis in the Hilbert space. One of the possible definitions is as follows

$$\hat{\rho} = \frac{1}{N} \sum_{i=1}^{N} |\Psi^i\rangle \langle \Psi^i|.$$

There are no restrictions on the states Ψ^i, these states can even be non-orthogonal, although it is usually not convenient. It is easy to show that if the basis of the eigenstates φ_n is chosen as the set of system eigenstates, this definition is equivalent to Eq. (30).

In order to give a more clear insight into the nature of the density matrix operator and reexpress it in an even more convenient form we introduce the so-called 'projector operators' (similar to those discussed in Section 3.2.2)

$$\hat{\pi}_\chi = |\chi\rangle \langle \chi|.$$

When acting on a state ψ these operators give a projection of the state ψ in the direction of the state χ. For the expectation value of the projector operator $\hat{\pi}_\chi$ in a state ψ one can easily obtain

$$\langle \hat{\pi}_\chi \rangle = \langle \psi | \hat{\pi}_\chi | \psi \rangle = \langle \psi | \chi \rangle \langle \chi | \psi \rangle = |\langle \chi | \psi \rangle|^2. \tag{32}$$

Eq. (32) gives the probability to find the system, which was originally prepared in the state $|\psi\rangle$, in the state $|\chi\rangle$.

Let us now return to the ensemble of emitters. Since the trace of an operator is independent of the basis in which this operator is defined, for convenience we will use the basis of the emitters eigenstates φ_n. In this case for the expectation value of the projector operator $\hat{\pi}_\chi$ one obtains

$$\overline{\langle \hat{\pi}_\chi \rangle} = \text{Tr}\{\hat{\pi}_\chi \hat{\rho}\} = \sum_n \langle \varphi_n | \chi \rangle \langle \chi | \hat{\rho} | \varphi_n \rangle = \sum_n \langle \chi | \hat{\rho} | \varphi_n \rangle \langle \varphi_n | \chi \rangle = \langle \chi | \hat{\rho} | \chi \rangle. \tag{33}$$

One can see that the probability of finding the ensemble of emitters in the state $|\chi\rangle$ is given by a diagonal element of the density matrix operator.

Now it is possible to make some generalization of the density matrix operator. Instead of defining the density matrix operator as a sum over all emitters states Ψ^i one can to use the sum over all states accessible to the ensemble elements

$$\hat{\rho} = \sum_j |\psi^j\rangle P(j) \langle \psi^j|. \tag{34}$$

Here $P(j)$ are the statistical weights which satisfy the requirement $\sum_j P(j) = 1$. A few paragraphs later, we explain the physical meaning of these coefficients in more details.

Using Eq. (33) and Eq. (34) we obtain the probability of finding the system in one of the states ψ^j which were used for the density matrix operator basis

$$\langle \psi^\alpha | \hat{\rho} | \psi^\alpha \rangle = \sum_j \langle \psi^\alpha | \psi^j \rangle P(j) \langle \psi^j | \psi^\alpha \rangle = \sum_j P(j) \left| \langle \psi^\alpha | \psi^j \rangle \right|^2. \tag{35}$$

If the set of states $|\psi^j\rangle$ is orthonormal, Eq. (35) can be simplified in the following way

$$\langle \psi^\alpha | \hat{\rho} | \psi^\alpha \rangle = \sum_j P(j) \delta_{\alpha j} = P(\alpha). \tag{36}$$

From the Eq. (36) one can see that the statistical weight $P(\alpha)$, in fact, defines the population of the state $|\psi^\alpha\rangle$ (i.e., probability that the state is occupied).

If the set $|\psi^j\rangle$ is not orthonormal, it is clearly not possible to obtain any simple relation between probabilities $\langle \psi^\alpha | \hat{\rho} | \psi^\alpha \rangle$ and statistical weights $P(\alpha)$.

3.2.5 Equation of motion for the density matrix

Coherent coupling: the von Neumann equation for the density matrix.

In Section 3.2.4 it was demonstrated that an average value of an observable O in an ensemble of emitters can be calculated using the system density matrix operator $\hat{\rho}$.

In the Schrödinger picture, all operators are time-independent and thus the time dynamics of the average should be hidden in the time dependence of the density matrix operator

$$\overline{\langle O_S \rangle}_t = \mathrm{Tr}\{\hat{\rho}(t)\hat{O}_S\},$$

where the index 'S' refers to the Schrödinger representation. It is clear that in order to be able to predict time dynamics of the system, an equation of motion for the density matrix operator is needed. Such an equation can be derived from the fact that the physical contents should not depend on whether the Schrödinger or Heisenberg picture is chosen for describing the system.

The density matrix operator $\hat{\rho}$ is defined as a sum of projections on a given set of states. In the Heisenberg picture the states are time-independent, though operators are time-dependent. In this case one can expect the density matrix operator to be defined by the initial state of the system. Comparing expressions for the observable averages in the Schrödinger and Heisenberg quantum mechanics descriptions we obtain

$$\overline{\langle O_{\mathrm{S}} \rangle}_t = \mathrm{Tr}\{\hat{\rho}(t)\hat{O}_{\mathrm{S}}\} = \overline{\langle O_{\mathrm{H}}(t) \rangle} = \mathrm{Tr}\{\hat{\rho}(t_0)\hat{O}_{\mathrm{H}}(t)\}, \tag{37}$$

where the index "H" refers to the Heisenberg representation. The evolution of operators in the Heisenberg picture can be related to the operators representation in the Schrödinger picture in the following way

$$\hat{O}_{\mathrm{H}}(t) = U^\dagger(t,t_0)\hat{O}_{\mathrm{S}}U(t,t_0). \tag{38}$$

In Eq. (38) $U(t,t_0)$ is the evolution operator given by

$$U(t,t_0) = \exp\left[-i\hat{H}(t,t_0)/\hbar\right],$$

where $\hat{H}$ is the system Hamiltonian. Substitution of Eq. (38) into Eq. (37) results in

$$\mathrm{Tr}\{\hat{\rho}(t)\hat{O}_{\mathrm{S}}\} = \mathrm{Tr}\{\hat{\rho}(t_0)U^\dagger(t,t_0)\hat{O}_{\mathrm{S}}U(t,t_0)\}.$$

Using the cycling property of the trace operation the equation above can be rewritten as

$$\mathrm{Tr}\{\hat{\rho}(t)\hat{O}_{\mathrm{S}}\} = \mathrm{Tr}\{U(t,t_0)\hat{\rho}(t_0)U^\dagger(t,t_0)\hat{O}_{\mathrm{S}}\}. \tag{39}$$

From Eq. (39) one can easily obtain the following expression for the density matrix operator time evolution

$$\hat{\rho}(t) = U(t,t_0)\hat{\rho}(t_0)U^\dagger(t,t_0). \tag{40}$$

Differentiation of Eq. (40) results in

$$i\hbar\frac{\partial\hat{\rho}(t)}{\partial t} = \left[i\hbar\frac{\partial U(t,t_0)}{\partial t}\right]\hat{\rho}(t_0)U^\dagger(t,t_0) - U(t,t_0)\hat{\rho}(t_0)\left[-i\hbar\frac{\partial U^\dagger(t,t_0)}{\partial t}\right]. \tag{41}$$

We simplify Eq. (41) using the fact that the evolution operator $U(t,t_0)$ satisfies the Schrödinger equation and obtain

$$i\hbar\frac{\partial\hat{\rho}(t)}{\partial t} = \hat{H}U(t,t_0)\hat{\rho}(t_0)U^\dagger(t,t_0) - U(t,t_0)\hat{\rho}(t_0)\hat{H}U^\dagger(t,t_0) = \hat{H}\hat{\rho}(t) - \hat{\rho}(t)\hat{H}. \tag{42}$$

Here Eq. (40) was used for the last step of the simplification. This equation of motion for the density matrix operator (mixed state) is called the 'von Neumann equation' [104]. It is an equivalent of the Schrödinger equation for the state vector (a pure state). The von Neumann equation can be written in a more compact form

$$\frac{\partial \hat{\rho}(t)}{\partial t} = \frac{i}{\hbar} \left[\hat{\rho}(t), \hat{H} \right]. \tag{43}$$

It should be stressed that the von Neumann equation corresponds to the Schrödinger quantum mechanics description, where all operators are time-independent. In the Heisenberg quantum mechanics description, the density operator does not depend on time and is defined by the initial conditions.

Incoherent processes: the Master Equation with the Linblad terms.

A correct description of a system which interacts with the external environment should include decoherence processes such as dissipation (decay) of particles to an external reservoir and income (pump) of particles from an external reservoir. In the case of the coupled 2LE-MC system these particles are either the MC photons, which can be supplied into the system, for instance, by the optical pumping, but eventually leak out, or the 2LE excitations, which can experience nonradioactive transitions from the excited to the ground state.

The leaking out photons not only cause decoherence in the system, but also provide an external observer with valuable information about the field-matter interaction inside the MC. This stresses once more the importance of considering the decoherence processes.

In order to account for the described processes the equation of motion for the density matrix operator should be upgraded from the von Neumann equation [104] to the master equation in the Lindblad form [105]

$$\frac{\partial \rho}{\partial t} = \frac{i}{\hbar}[\rho, H_{JC}] + \mathscr{L}_P^{MC}\rho + \mathscr{L}_\gamma^{MC}\rho + \mathscr{L}_\gamma^{2LE}\rho, \tag{44}$$

In Eq. (44) $H_{JC} = H_{MC} + H_{2LE} + H_{INT}$ is the full Hamiltonian of the coupled 2LE-MC system first introduced by *Jaynes and Cummings* [106] and now commonly called 'Jaynes-Cummings Hamiltonian' with H_{MC} given by Eq. (12), H_{2lE} given by Eq. (19), and H_{INT} given by Eq. (26). The operators $\mathscr{L}_P^{MC}$, $\mathscr{L}_\gamma^{MC}$, and $\mathscr{L}_\gamma^{2LE}$ are the so-called Lindblad terms. In the explicit form these three terms are given by

$$\mathscr{L}_P^{MC}\rho = \frac{P_{MC}}{2}(2a^\dagger \rho a - aa^\dagger \rho - \rho aa^\dagger + 2a\rho a^\dagger - a^\dagger a\rho - \rho a^\dagger a),$$

$$\mathscr{L}_\gamma^{MC} rho = \frac{\gamma_{MC}}{2}(2a\rho a^\dagger - a^\dagger a\rho - \rho a^\dagger a),$$

and

$$\mathscr{L}_\gamma^{2LE}\rho = \frac{\gamma_{2LE}}{2}(2\sigma \rho \sigma^\dagger - \sigma^\dagger \sigma \rho - \rho \sigma^\dagger \sigma),$$

where P_{MC} is the intensity of the MC pumping, γ_{MC}, γ_{2LE} are the decaying rates of the MC and 2LE excitation, $a^\dagger$, a are MC creation and annihilation operators (the same that enter H_{MC}, see Eq. (12)), and $\sigma^\dagger$, σ are 2LE creation and annihilation operators (the same that enter H_{2LE}, see Eq. (19)).

In the scope of this chapter we are not interested in particular pumping and dissipation mechanisms which are present in various experimental systems. We only note that different pumping and dissipation process were studied by a number of authors, see, e.g., Refs. [107, 108]. For our further considerations only the fact that all such processes are well-described by the introduced master equation with Lindblad terms is important.

Mainly, there are two different derivations of the Lindblad terms in Eq. (44) which can be found in the literature. The first derivation is based on a microscopic study of the system coupling to an external reservoir, which is represented as a bath of oscillators [94, 109]. The second procedure utilizes the Monte-Carlo method and quantum jumps. This approach is preferred in Refs. [89, 90] as it is closer to the quantum information and measurement theories. In this case, the time evolution of the system is understood as a sequence of coherent periods of the Hamiltonian dynamics and incoherent events taking place with some probability. In this picture the microscopic origin of the incoherent processes is not considered and they are just assumed to be present with a given probability.

All together, the Lindblad terms $\mathscr{L}_P^{MC}$, $\mathscr{L}_\gamma^{MC}$, and $\mathscr{L}_\gamma^{2LE}$ can be put in the form of a total superoperator $\mathscr{L}$

$$\frac{\partial \rho}{\partial t} = \frac{i}{\hbar}[\rho, H] + \mathscr{L}\rho.$$

Due to the balance between the pump and decay, after some time a steady state is established. We denote the density matrix which describes such steady state by ρ^{SS}. Throughout this chapter we consider only such values of the parameters P_{MC}, γ_{MC}, and γ_{2LE} which lead to establishing of some steady state with non-divergent populations. We do not discuss exact experimental conditions which result in a particular combination of these parameters and only note that all the considered values of P_{MC}, γ_{MC}, and γ_{2LE} correspond to attainable experimental systems.

3.3 Calculating optical transitions: electric dipole approximation

Let us consider a system described by the full Hamiltonian $H(t) = H^0 + H'(t)$ where H^0 is the stationary (time-independent) Hamiltonian with eigenfunctions $|\psi_j\rangle$ satisfying

$$H^0 |\psi_j\rangle = \varepsilon_j |\psi_j\rangle,$$

with $\varepsilon_j = \hbar\omega_j$, and $H'(t)$ is the time-dependant perturbation given by

$$H'(t) = \tilde{H}' e^{-i\omega t},$$

where ω is the frequency of the exciting radiation. If perturbation is weak, it only causes transitions between the states $|\psi_j\rangle$. According to the first order time-dependant perturbation theory the rate of transitions between two different states

$|\psi_i\rangle$ (initial state) and $|\psi_f\rangle$ (final state) is given by

$$T_{if} = \frac{1}{\hbar^2} \left| \langle \psi_f | H'(t) | \psi_i \rangle \right|^2 \frac{\sin^2 \left[\frac{\tau}{2} \left(\omega_f - \omega_i - \omega \right) \right]}{\tau \left[\frac{1}{2} \left(\omega_f - \omega_i - \omega \right) \right]^2}.$$

Here τ is the time which corresponds to the broadening of the optical transitions and which can be defined as $\tau \geq 2\pi/\Delta\omega$ where $\Delta\omega$ is the linewith of the excitation radiation. If $\Delta\omega$ is small, τ becomes large and using

$$\delta(\xi) = \lim_{x \to 0} \frac{x}{\pi} \frac{\sin^2(\xi/x)}{\xi^2}$$

we obtain the rate of transitions between the system eigenstates $|\psi_i\rangle$ and $|\psi_f\rangle$ given by Fermi's golden rule

$$T_{if} = \frac{2\pi}{\hbar} \left| \langle \psi_f | H'(t) | \psi_i \rangle \right|^2 \delta(\varepsilon_f - \varepsilon_i - \hbar\omega). \tag{45}$$

The Hamiltonian operator of an electron interacting with electromagnetic field is given by

$$H = \frac{1}{2m} \left(\mathbf{p} + \frac{q}{c} \mathbf{A} \right)^2 = H^0 + \frac{q}{2mc} \left(\mathbf{A} \cdot \mathbf{p} + \mathbf{p} \cdot \mathbf{A} \right) + \frac{1}{2m} \left(\frac{q}{c} \right)^2 \mathbf{A} \cdot \mathbf{A}, \tag{46}$$

where $H^0 = \mathbf{p}/2m$ is the Hamiltonian of the unperturbed system, m is the electron mass, $\mathbf{p}$ is the electron momentum operator, and $\mathbf{A}$ is the electromagnetic field vector potential.

The vector potential of a plane electromagnetic wave, hitting the sample at normal incidence, can be chosen as

$$\mathbf{A} = \mathbf{A_0} \cos(\mathbf{Q}\mathbf{r} - \omega t),$$

where $\mathbf{Q}$ is the field wave vector and $\mathbf{r}$ is the position vector. The electric field of the perturbing radiation is calculated as the time derivative of the vector potential

$$\mathbf{E}(\mathbf{r},t) = \frac{1}{c} \frac{\partial \mathbf{A}(\mathbf{r},t)}{\partial t}.$$

In the Coulomb gauge the vector potential of a sourceless electromagnetic field in vacuum satisfied $\nabla \cdot \mathbf{A} = 0$ and therefore

$$[\mathbf{A}, \mathbf{p}] = i\hbar\nabla \cdot \mathbf{A} = 0.$$

The ratio of the third to the second term in Eq. (46) can be written in the following way

$$\frac{e}{c} \frac{A}{p} = \frac{eE}{\omega p} \approx \frac{e}{\omega p} \left(\frac{8\pi S}{c} \right)^{1/2} \tag{47}$$

where E is the magnitude of the electric field associated with the perturbing radiation and S is the Poynting vector, which gives energy flux density of the electromagnetic field (energy per time per unit area). Expression in Eq. (47) is much less than unity for the values of S up to 10^{12}W/m^2. For most material such field intensities are higher than the material damage threshold. Thus, the third term in Eq. (46) can be safely neglected

$$H = H^0 + \frac{q}{mc}(\mathbf{A} \cdot \mathbf{p}) + \frac{1}{2m}\left(\frac{q}{c}\right)^2 \mathbf{A} \cdot \mathbf{A} \approx H^0 + \frac{q}{mc}(\mathbf{A} \cdot \mathbf{p}).$$

The second term in this equation can be easily expressed as $H_+ e^{-i\omega t} + H_- e^{i\omega t}$ with $H_\pm$ given by

$$H_\pm = \frac{q}{2mc} e^{\pm i\mathbf{Q}\mathbf{r}} \mathbf{A_0} \cdot \mathbf{p} = \frac{q}{2mc} |\mathbf{A_0}| e^{\pm i\mathbf{Q}\mathbf{r}} (\mathbf{e} \cdot \mathbf{p}),$$

where we have introduced the radiation polarization vector $\mathbf{e}$ and the vector $\mathbf{r}$ should be taken at the position of the electron.

To simplify calculations we use the dipole approximation, which assumes that $\mathbf{Q}\mathbf{r} \ll 1$ and thus $e^{\pm i\mathbf{Q}\mathbf{r}} \approx 1$. Within this approximation $H_\pm$ becomes

$$H_\pm = \frac{q}{2mc} |A_0| (\mathbf{e} \cdot \mathbf{p}). \tag{48}$$

Substituting Eq. (48) into Eq. (45) (the Fermi's golden rule) we get the final expression for the rate of optical transitions between the states $|\psi_i\rangle$ and $|\psi_f\rangle$ caused by the perturbing electromagnetic field

$$T_{if} = \frac{2\pi}{\hbar}\left(\frac{q}{2mc}\right)^2 |A_0|^2 \left|\langle \psi_f | \mathbf{e} \cdot \mathbf{p} | \psi_i \rangle\right|^2 \delta(\varepsilon_f - \varepsilon_i - \hbar\omega).$$

4 Quantum rings in classical electromagnetic fields. Electric Dipole Moment Oscillations and Terahertz Transitions in Aharonov-Bohm Quantum Rings.

4.1 Introduction

Recently a lot of attention has been turned towards non-simply-connected nanostructures, quantum rings, which have been obtained in various semiconductor systems [9, 10, 17]. The fascination in quantum rings is partially caused by a wide variety of purely quantum mechanical effects, which are observed in ring-like nanostructures. The star amongst them is the Aharonov-Bohm effect [1, 39], in which a charged particle is influenced by a magnetic field away from the particle's trajectory, resulting in magnetic-flux-dependent oscillations of the ring-confined particle energy. The oscillations of the single-particle energy are strongly suppressed by distortion of the ring shape or by applying an in-plane (lateral) electric field, thus re-

ducing the symmetry of the system [110, 111] (see Fig. 1). However, there are other
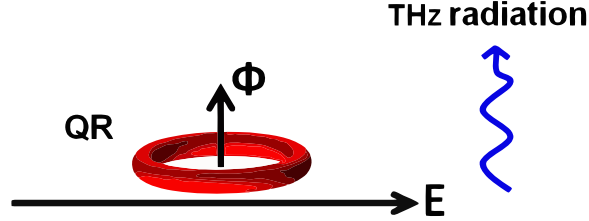
Fig. 1 An Aharonov-Bohm quantum ring pierced by a magnetic flux and subjected to a lateral electric field. (From Ref. [3]).

physical quantities, which might have even more pronounced magneto-oscillations when the symmetry of the ring is reduced. For example, in the presence of a lateral electric field exceeding a particular threshold it is possible to switch the ground state of an exciton in an Aharonov-Bohm ring from being optically active (bright) to optically inactive (dark)[62, 18]. Another hitherto overlooked phenomenon is the flux-periodic change of an electric dipole moment of a quantum ring, which is the main subject of this work.

This section is organized as follows. In Section 4.2 we calculate the single-electron energy spectrum of an infinitely-narrow Aharonov-Bohm ring subjected to a lateral electric field. In Section 4.3 we consider magneto-oscillations of the ring's electric dipole moment and study their electric field and temperature dependence. Matrix elements of the dipole moment calculated between different states define selection rules for optical transitions. For experimentally attainable quantum rings these transitions occur at THz frequencies. In Section 4.4 we discuss optical selection rules for intraband optical transitions and show how the polarization properties of the associated THz radiation can be tuned by external electric and magnetic fields. Section 4.5 contains a brief discussion of the potential applications of the predicted phenomena.

4.2 Energy spectrum of an infinitely-narrow quantum ring

4.2.1 Magneto-oscillations of the quantum ring eigenenergies

The Hamiltonian of an electron confined in an infinitely narrow QR pierced by magnetic flux Φ depends only on the polar coordinate φ

$$H_\Phi = -\frac{\hbar^2}{2M_e R^2} \frac{\partial^2}{\partial \varphi^2} - \frac{i\hbar e}{2\pi} \frac{\Phi}{M_e R^2} \frac{\partial}{\partial \varphi} + \frac{e^2 \Phi^2}{8\pi^2 M_e R^2} ,$$

(49)

where M_e is the electron effective mass and R is the QR radius. The 2π-periodic eigenfunctions of the Hamiltonian defined by Eq. (49) are

$$\psi_m(\varphi) = \frac{e^{im\varphi}}{\sqrt{2\pi}}, \qquad (50)$$

and the corresponding eigenvalues are given by

$$\varepsilon_m(f) = \frac{\hbar^2 (m+f)^2}{2M_e R^2} = (m+f)^2 \varepsilon_1(0). \qquad (51)$$

Here $m = 0, \pm 1, \pm 2...$ is the angular momentum quantum number, and $f = \Phi/\Phi_0$ is the number of flux quanta piercing the QR ($\Phi_0 = h/e$). The electron energy spectrum defined by Eq. (51) is plotted in Fig. 2. It exhibits oscillations in magnetic
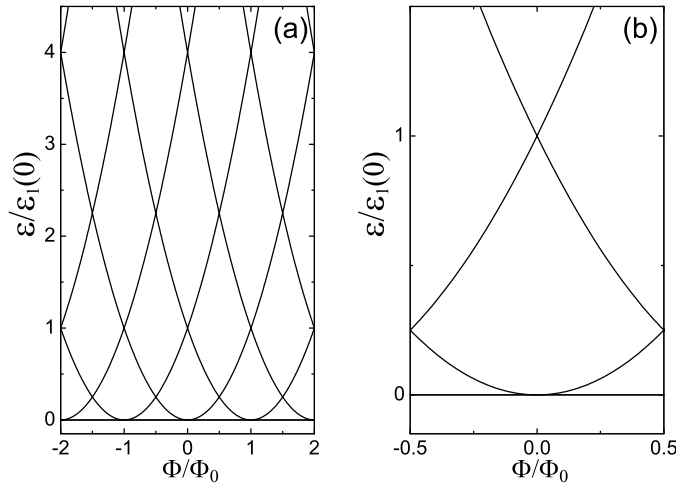
Fig. 2 (a) The energy spectrum of an infinitely narrow quantum ring pierced by a magnetic flux Φ. Each parabola corresponds to a particular value of the electron angular momentum m. The electron energies ε are plotted versus the number of flux quanta Φ/Φ_0. (b) Expanded view on a smaller energy scale. (From Ref. [3]).

flux with the period equal to Φ_0, known as Aharonov-Bohm oscillations [9, 1]. One can see intersections (degeneracy) of the energy levels with different angular momenta, when Φ is equal to an integer number of $\Phi_0/2$. Optical selection rules allow transitions between states with angular momentum quantum numbers different by unity ($\Delta m = \pm 1$). For typical nanoscale rings [9, 10] the energy scale of the interlevel separation, $\varepsilon_1(0) = \hbar^2/2M_e R^2$, is in the THz range. When Φ exceeds $\Phi_0/2$ the electron possesses a non-zero angular momentum in the ground state.

4.2.2 Energy spectrum in the presence of a lateral electric field

Applying an in-plane electric field **E** removes the circular symmetry of the system. An additional term corresponding to the electric field appears in the Hamiltonian [3, 2], which acquires a form

$$H = H_\Phi + eER\cos\varphi. \qquad (52)$$

Now the angle φ is counted from the direction of the electric field (geometry of the problem is shown in Fig. 3). The field mixes electron states with different angular
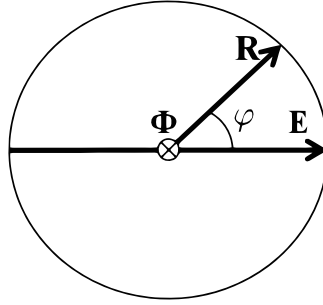
Fig. 3 Relative directions of the external electric field **E** and the electron position vector **R**. (From Ref. [3]).

momentum, which is not a good quantum number anymore. An eigenfunction of the Hamiltonian (52), which maintains the 2π-periodicity in φ, can be written as a linear combination of the wavefunctions (50)

$$\Psi_n(\varphi) = \sum_m c_m^n e^{im\varphi}. \qquad (53)$$

Substituting the wavefunction (53) into the Schrödinger equation with the Hamiltonian (52), multiplying the resulting expression by $e^{-im\varphi}$ and integrating with respect to φ leads to an infinite system of linear equations for the coefficients c_m^n

$$\left[(m+f)^2 - \lambda_n\right] c_m^n + \beta\left(c_{m+1}^n + c_{m-1}^n\right) = 0, \qquad (54)$$

where $\beta = eER/2\varepsilon_1(0)$ and $\lambda_n = \varepsilon_n/\varepsilon_1(0)$, with ε_n being the nth eigenvalue of the Hamiltonian (52). It is apparent from Eq. (54) that all the properties of the ring are periodic in magnetic flux. Therefore, it is sufficient to consider $0 \leq f \leq 1/2$, whereas the calculations for other values of f can be performed by shifting m in Eq. (54) by an integer number. Interestingly, exactly the same analysis is applicable to a nanohelix subjected to an electric field normal to its axis [112, 113, 114]. For a

helix the role of magnetic flux is played by the electron momentum along the helical line.

It should be emphasized that we consider a single-electron problem and we are interested only in a few low-energy states. This treatment is relevant to nanoscale-sized semiconductor QRs or type-II QDs discussed in Refs. [9, 10, 17, 36, 62, 18] and neglects the many-body effects which are known to influence Aharonov-Bohm oscillations in mesoscopic rings [34, 35]. The energy levels ε_n as well as the coefficients c_m^n can be found by cutting off the sum in Eq. (53) at a particular value of $|m|$. The results of the numerical diagonalization of the matrix corresponding to the system of linear equations (54), with a cut-off value of $|m| = 11$, are plotted in Fig. 4. The same cut-off value was chosen in all numerical calculations presented in this
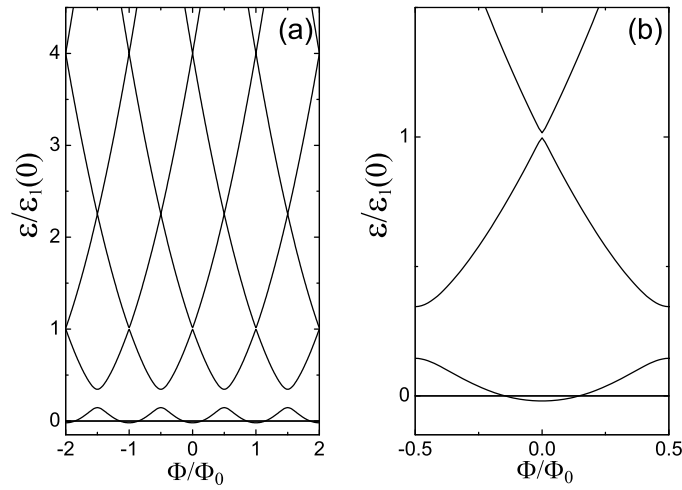
Fig. 4 (a) The energy spectrum of an infinitely narrow quantum rings of radius R pierced by a magnetic flux Φ and subjected to an in-plane electric field $E = 0.2\varepsilon_1(0)/eR$. The electron energies ε are plotted versus the number of flux quanta Φ/Φ_0. (b) Expanded view on a smaller energy scale. (From Ref. [3]).

section, since a further increase of the matrix size does not lead to any noticeable change in the results for the three lowest-energy states, which we are interested in.

In small electric fields, $eER \ll \hbar^2/2M_eR^2$, a significant change in the QR energy spectrum occurs only for the ground and two lowest excited states, when Φ is close to an integer number of $\Phi_0/2$ (the points of degeneracy in the absence of the electric field). The most prominent change is associated with the linear in electric field splitting between the ground and first excited states for half-integer f. The less pronounced quadratic in electric field splitting between the first and second excited states occurs for integer f. These splittings can be easily understood with the help of perturbation theory, as there is a non-zero matrix element of $eER\cos\varphi$ between the ground and the first excited state, whereas the two excited states are only repelled

in the second order via the ground state. It is shown in Appendix 6.2, these essential features of the low-energy spectrum are fully captured by considering small-size matrices, which allow an analytical treatment: a two-by-two matrix for half-integer f and a three-by-three matrix for integer f.

As one can see from Fig. 4, energy oscillations in the ground state are strongly suppressed even for $eER = 0.2\hbar^2/2M_eR^2$. This suppression is a major source of difficulty in spectroscopic detection of Aharonov-Bohm oscillations. However, as we show in the next two Sections, apart from the ground-state energy there are other physical quantities, such as a dipole moment of the QR and polarization properties of the inter-level transitions, which have highly-pronounced magneto-oscillations when the symmetry of the ring is reduced.

4.3 Magneto-oscillations of the quantum ring electric dipole moment

In this Section we consider Aharonov-Bohm oscillations of the QR electric dipole moment. If an electron occupies the nth state of the neutral single-electron QR with a uniform positive background, or if a positive charge $+e$ is placed at the center of the QR (geometry of the problem is shown in Fig. 3), the projection of the dipole moment on the direction of the lateral electric field [3, 2] is given by

$$P_n = eR \int |\Psi_n|^2 \cos\varphi \, d\varphi. \tag{55}$$

Substituting the wavefunction (53) into Eq. (55) yields the following expression for P_n

$$P_n = \frac{eR}{2} \sum_m c_m^n \left(c_{m-1}^n + c_{m+1}^n \right), \tag{56}$$

where the coefficients c_m^n can be found from the system of linear equations (54). In the absence of an electric field, each of the electron states is characterized by a particular value of angular momentum. The electron charge density is spread uniformly over the ring and there is no net dipole moment. The same result is given by Eq. (56) - all the products $c_m^n c_{m\pm 1}^n$ entering Eq. (56) vanish for any value of n resulting in the QR dipole moment being equal to zero. Let us now consider what happens to the ground state's dipole moment in the presence of a weak electric field, $eER << \hbar^2/2M_eR^2$. For $\Phi = 0$, the ground state is a practically pure $m = 0$ state with a tiny admixture of $m \neq 0$ wavefunctions. However, the situation changes drastically near the points of degeneracy when the magnetic flux through the QR is equal to any odd integer of $\Phi_0/2$. For a half-integer flux, even an infinitely small field modifies entirely the wavefunction of the ground state. As shown in Appendix 6.2, when $f = 1/2$ the ground state wavefunction angular dependence is well-described by $\sin(\varphi/2)$. Thus, the ground state electron density distribution becomes shifted to one side of the ring, in the opposite direction to the applied electric field. Such a

shift is energetically favorable and results in the value of the dipole moment being close to eR. Simultaneously, the first excited state wavefunction angular dependence becomes well-described by $\cos(\varphi/2)$. For the excited state, the electron is localized near the opposite side of the ring resulting in a dipole moment of the same magnitude as for the ground state but with the opposite sign.

The electron density distributions in the ground and first excited states, when $\Phi = 0$ and $\Phi = \Phi_0/2$ and the degeneracy is lifted by a weak electric field, is shown in Fig. 5. With changing magnetic flux the ground state density oscillates with a
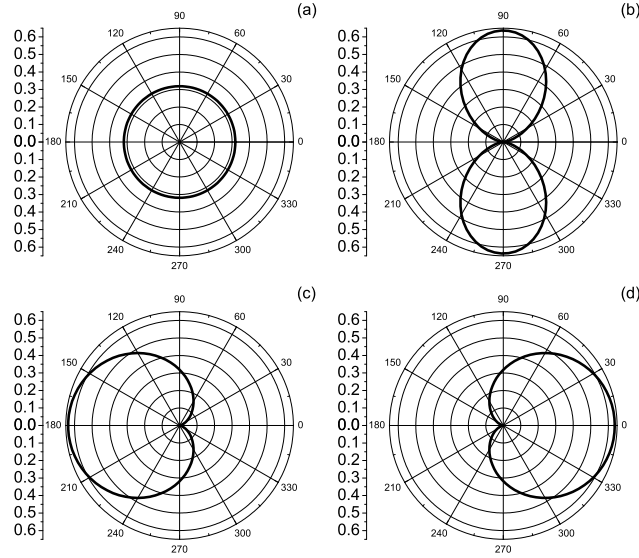
Fig. 5 A polar plot of the electron density distribution in a single-electron quantum ring pierced by the magnetic flux $\Phi = 0$ (top row) and $\Phi = \Phi_0/2$ (bottom row) and subjected to a weak in-plane electric field, $E \ll \varepsilon_1(0)/eR$: (a) and (c) for the electron ground state; (b) and (d) for the first excited state. (From Ref. [3]).

period Φ_0 from an unpolarized to a strongly polarized distribution, resulting in the corresponding dipole moment oscillations. However, the oscillations of the total dipole moment of the QR should be partially compensated if the first excited state, which carries a dipole moment opposite to the ground state's dipole moment for a flux equal to an odd number of $\Phi_0/2$, is also occupied due to a finite temperature. The effect of temperature T can be taken into account by thermal averaging over all states

$$\langle P \rangle = \frac{\sum_n P_n \exp(-\varepsilon_n/k_{\mathbf{B}}T)}{\sum_n \exp(-\varepsilon_n/k_{\mathbf{B}}T)}. \tag{57}$$

The results of numerical calculations, using Eq. (57), for several temperature values are shown in Fig. 6. The dipole moment oscillations, which are well-pronounced for $k_{\mathrm{B}}T \ll eER$, become suppressed when the temperature increases.
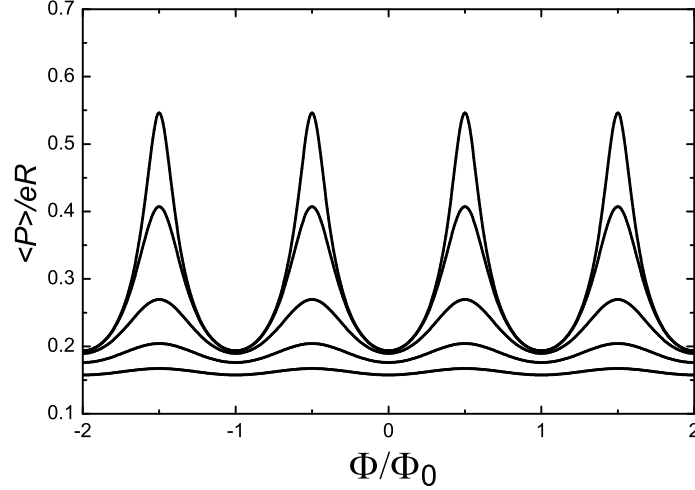
Fig. 6 Magneto-oscillations of the dipole moment of a ring at various temperatures for $E = 0.2\varepsilon_1(0)/eR$. Different curves correspond to different temperatures in the range from $T = 0.01\varepsilon_1(0)/k_{\mathbf{B}}$ to $T = 0.41\varepsilon_1(0)/k_{\mathbf{B}}$ with the increment $0.1\varepsilon_1(0)/k_{\mathbf{B}}$. The upper curve corresponds to $T = 0.01\varepsilon_1(0)/k_{\mathbf{B}}$. (From Ref. [3]).

In this work we consider the limit of weak electric field only. Higher fields, $eER > \hbar^2/2M_eR^2$, localize the ground state electron near one side of the ring even in the absence of a magnetic field and the change of magnetic flux through the QR can no longer influence the electron density distribution. For all values of Φ the ground state wavefunction consists of a mixture of functions with different angular momenta, ensuring that this state is always strongly polarized. The suppression of the dipole moment oscillations with increasing electric field can be seen in Fig. 7 where the upper curves, corresponding to higher electric fields and higher dipole moments, exhibit less pronounced oscillations. The energy oscillations for several lowest states are known to be completely suppressed in strong electric fields [111].

At this point it is instructive to discuss conditions needed for an experimental observation of electric dipole moment magneto-oscillations in QRs. A typical radius for experimentally attainable QRs [9, 10, 17] is $R \simeq 20\,\mathrm{nm}$. This gives the characteristic energy scale of the inter-level separation $\varepsilon_1(0) \simeq 2\,\mathrm{meV}$ (corresponding to 0.5THz) for an electron of effective mass $M_e = 0.05m_e$. For a ring with $R = 20\,\mathrm{nm}$, the magnitude of a magnetic field producing a flux $\Phi = \Phi_0$ is $B \simeq 3\,\mathrm{T}$. Therefore, a further decrease of the QR radius would require magnetic fields which are hard to achieve. A typical electric field needed for pronounced dipole moment
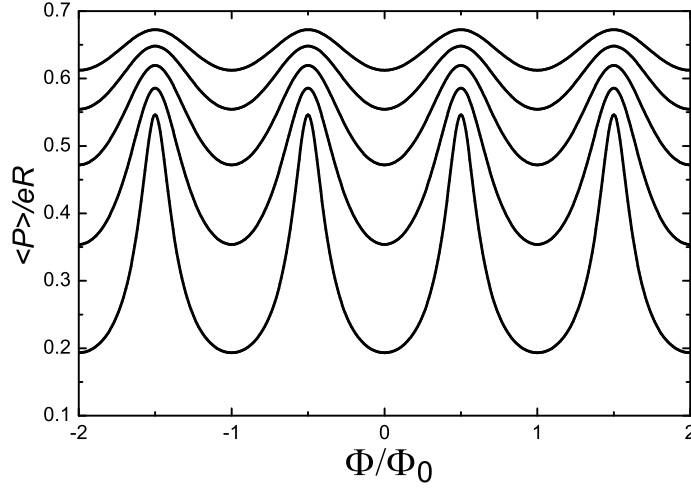
Fig. 7 Magneto-oscillations of the dipole moment of a ring at various magnitudes of the in-plane electric field for $T = 0.01\varepsilon_1(0)/k_B$. Different curves correspond to different magnitudes of the electric field in the range from $E = 0.2\varepsilon_1(0)/eR$ to $E = 1.0\varepsilon_1(0)/eR$ with the increment $0.2\varepsilon_1(0)/eR$. The upper curve corresponds to $E = 1.0\varepsilon_1(0)/eR$. (From Ref. [3]).

oscillations is $E = 0.1\varepsilon_1(0)/eR \simeq 10^4\,\mathrm{V/m}$, which can be easily created. By far the most difficult condition to be satisfied is the requirement on the temperature regime, $T < eER/k_B$. For the discussed electric field and ring radius this condition becomes $T < 2\mathrm{K}$. In principle such temperatures can be achieved in laboratory experiments and magneto-oscillations can be detected, for example, in capacitance measurements. However, for practical device applications, such as quantum-ring-based magnetometery, higher temperatures are desirable. In the next section we consider a process, which is less sensitive to the temperature-induced occupation of excited states.

## 4.4 Terahertz transitions and optical anisotropy in quantum rings

In this Section we study the influence of the in-plane electric field on polarization properties of radiative inter-level transitions in Aharonov-Bohm QRs. We restrict our consideration to linearly-polarized radiation and dipole optical transitions only[1]. The case of circular polarization is briefly discussed at the end of the Section.

---

[1] For the theoretical background on the electric dipole approximation for optical transitions please see Section 3.3 of this chapter.

The transition rate T_{if} between the initial (i) and final (f) electron states is governed by the matrix element $P_{if} = \langle f|\mathbf{e}\hat{\mathbf{P}}|i\rangle$, where $\hat{\mathbf{P}}$ is the dipole moment operator and $\mathbf{e}$ is the projection of the radiation polarization vector onto the plane of the QR. For the model of an infinitely-narrow QR

$$P_{if}(\theta) = eR \int \Psi_f^* \Psi_i \cos(\theta - \varphi)\, d\varphi, \tag{58}$$

where θ is the angle between the vector $\mathbf{e}$ and the in-plane electric field $\mathbf{E}$. The geometry of the problem is shown in Fig. 8.
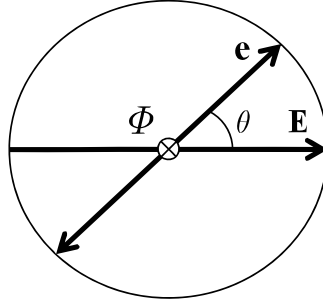
Fig. 8 Relative directions of the external electric field $\mathbf{E}$ and the projection $\mathbf{e}$ of the THz radiation polarization vector onto the quantum ring's plane. (From Ref. [3]).

Substituting the electron wavefunctions Ψ_i and Ψ_f, given by Eq. (53), into Eq. (58) yields

$$T_{if} \sim P_{if}^2(\theta) = P_{if}^{-2} + P_{if}^{+2} - 2P_{if}^- P_{if}^+ \cos 2\theta, \tag{59}$$

where

$$P_{if}^- = \frac{eR}{2}\left|\sum_m c_m^f c_{m-1}^i\right| \tag{60}$$

and

$$P_{if}^+ = \frac{eR}{2}\left|\sum_m c_m^f c_{m+1}^i\right|. \tag{61}$$

The double angle 2θ entering Eq. (59) ensures that the transition rate does not depend on the sign of $\mathbf{e}$.

Let us consider transitions between the ground state and the first excited state of the Aharonov-Bohm QR in the limit of a weak in-plane electric field, $eER \ll \hbar^2/2M_e R^2$. Away from the points of degeneracy the ground and the first excited states are characterized by a particular value of m and either P_{if}^- or P_{if}^+ given by Eqs. (60)-(61) vanishes. As a result, the angular dependence in Eq. (59) disappears and the transitions have no linear polarization. The picture changes drastically when Φ is equal to an integer number of $\Phi_0/2$. Then $P_{if}^- = P_{if}^+$ and therefore the rate of

transitions induced by the radiation polarized parallel to the direction of the in-plane electric field ($\theta = 0$) is equal to zero, $T_{if} = T_{\parallel} = 0$. Simultaneously $T_{\perp}$, the rate of transitions induced by the light polarized perpendicular to the direction of the in-plane electric field ($\theta = \pi/2$), reaches its maximum possible value. This leads to the strong optical anisotropy of the system. The results of the calculations for the whole range of Φ are shown in Fig. 9. Very sharp peaks at Φ equal to an integer
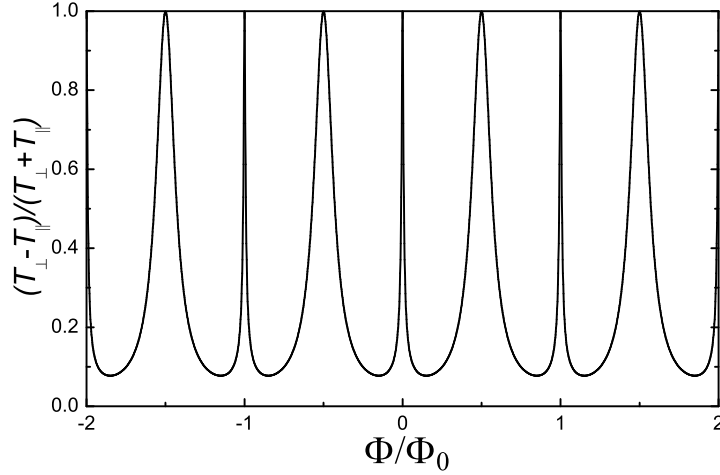
Fig. 9 Magneto-oscillations of the degree of polarization for the transitions between the ground state and the first excited state. Here $T_{\parallel}$ and $T_{\perp}$ correspond to the intensities of transitions polarized parallel ($\mathbf{e} \parallel \mathbf{E}$) and perpendicular ($\mathbf{e} \perp \mathbf{E}$) to the direction of the in-plane electric field, respectively. (From Ref. [3]).

number of Φ_0 are the result of splitting between the first and second excited states, which were degenerate with energy $\varepsilon_1(0)$ in the absence of an external electric field (see Fig. 4). This splitting occurs in the second order in eER and the spectacular sharpness of the peaks is due to the very fast change in the electron first and second excited states wavefunctions when one moves away from the point of degeneracy (for details see Appendix 6.2). The optical transitions between the electron ground and second excited states are also linearly polarized, but with $\theta = 0$, so that the polarization of these transitions is normal to the polarization of transitions between the electron ground and first excited states. Because these two peaks are very closely separated for $\Phi = 0$, the polarization effects are strongly suppressed if the finite linewidth of the radiation is taken into account.

In the case of circularly polarized light, the degree of polarization oscillates as well. Inter-level transitions between the 'pure' states, characterized by the definite angular momentum values differing by one, are either right-hand or left-hand polarized. However, one can easily see that transitions involving the states, which are

strongly 'mixed' when the flux is an integer number of $\Phi_0/2$, have the same proba- bilities for both circular polarizations. Thus, the magnetic-field-induced optical chi- rality of QRs oscillates with the flux.

The total probabilities of the inter-level transitions indeed depend on the pop- ulations of the states involved. However, the discussed oscillations of the degree of polarization do not depend on temperature as the selection rules for the optical transitions are temperature-independent. This effect allows Aharonov-Bohm rings to be used as room-temperature polarization-sensitive detectors of THz radiation or optical magnetometers.

4.5 Results and discussion

It is demonstrated that a lateral electric field, which is known to suppress Aharonov- Bohm oscillations in the ground state energy spectrum of a QR, results in strong oscillations of other physical characteristics of the system. Namely, the electric- field-induced dipole moment oscillates as a function of the magnetic flux piercing the QR, with pronounced maxima when the flux is equal to an odd number of one half of the flux quantum. This effect is caused by lifting the degeneracy of states with different angular momentum by arbitrary small electric fields. It should be empha- sized that the discussed effect is not an artifice of the infinitely-narrow ring model used in the calculations, but it persists in finite-width rings in a uniform magnetic field. Indeed, the essential feature required for this effect is the degeneracy of the states with the angular momenta differing by one at certain magnetic field values, which is known to take place for finite-width rings as well [57, 58, 59, 60, 115].

Future observation of the dipole moment magneto-oscillations would require careful tailoring of the QR parameters and experiment conditions. For example, the size of the QR should not exceed the electron mean free path but should be large enough so that, for experimentally attainable magnetic fields, the flux through the ring is near the flux quantum. The electric field should not be too large to avoid polarizing the QR strongly in the absence of a magnetic field, but it should be large enough to achieve a splitting between the ground and first excited states exceeding $k_{\mathrm{B}}T$. Estimates presented in this section show that all these conditions can be met in existing QR systems. However, the temperature constraint constitutes the major obstacle for any potential applications outside the low-temperature laboratory.

The temperature restrictions are less essential for another predicted effect - giant magneto-oscillations of the polarization degree of radiation associated with inter- level transitions in Aharonov-Bohm QRs. Notably, these transitions for the QRs satisfying the remaining constraints should occur at THz frequencies. Creating re- liable, portable and tunable sources of THz radiation is one of the most formidable problems of contemporary applied physics. The unique position of the THz range in between the frequencies covered by existing electronic or optical mass-produced devices results in an unprecedented variety of ideas aiming to bridge the so-called 'THz gap'. For example, the proposed methods of down-conversion of optical exci-

tation range from creating ultra-fast saturable absorbers [116] to utilizing magnetic-field-induced energy gap in metallic carbon nanotubes [117, 118, 119, 120] to recent proposals of exciting THz transitions between exciton-polariton branches in semi-conductor microcavities [121, 122, 123]. Arguably, the use of QRs for THz generation and detection has its merits, since their electronic properties can be easily tuned by external fields. The following scheme for using Aharonov-Bohm QRs as tuneable THz emitters can be proposed. Inversion of population in semiconductor QRs or type II QDs can be created by optical excitation across the semiconductor gap. Angular momentum and spin conservation rules do not forbid the creation of an electron in the first excited state as long as the total selection rules for the whole system, consisting of an electron-hole pair and a photon causing this transition, are satisfied. Terahertz radiation will be emitted when the electron undergoes a transition from the excited to the ground state of the QR. As was shown in the previous Sections both the frequency and polarization properties of this transition can be controlled by external magnetic and electric fields.

Other potential applications of the discussed effects are in the burgeoning areas of quantum computing and cryptography. The discussed mixing of the two states, which are degenerate in the absence of electric field, is completely controlled by the angle between the in-plane field and a fixed axis. This brings the potential possibility for creating nanoring-based qubits, which do not require weak spin-orbit coupling between the electric field and electron spin. Arrays of the Aharonov-Bohm QRs can also be used for polarization sensitive single-photon detection, which is essential for quantum cryptography.

5 Quantum rings in quantized electromagnetic fields. Aharonov-Bohm Quantum Rings Embedded Into High-Quality Terahertz Microcavities.

5.1 Introduction

Progress in nanolithography and epitaxial techniques has resulted in burgeoning developments in the fabrication of micro-scale optical resonators, known as optical microcavities. If the quality factor of a cavity is sufficiently large, the formation of hybrid light-matter excitations occurs. Being first observed two decades ago [124], the strong coupling regime is now routinely achieved in different kinds of microcavities [125]. From the point of view of fundamental physics, this regime is interesting for investigation of various collective phenomena in condensed matter systems such as the high-temperature Bose-Einstein condensation (BEC) [126, 127] and superfluidity [128]. From the viewpoint of applications it opens a way towards to the realization of optoelectronic devices of the next generation [129]: room-temperature polariton lasers [130], polarization-controlled optical gates, [131], effective sources of THz radiation [132, 123, 121], and others.

Several applications of the strong coupling regime were also proposed for quantum information processing [133, 134, 135]. In this case one should be able to tune the number of emitted photons in a controllable way. This is hard to achieve in planar microcavities, where the number of elementary excitations is macroscopically large, but is possible in microcavities containing single quantum dots, where the quantum dot exciton can be coupled to a confined electromagnetic mode provided by a micropillar (etched planar cavity) [80], a defect of the photonic crystal [79], or a whispering gallery mode [81, 136]. That is why the strongly coupled systems based on quantum dots have attracted particular attention recently. In the strong coupling regime the system possesses a rich multiplet structure, which maps transitions between quantized dressed states of the light-matter coupling Hamiltonian [80, 79, 81, 82, 102, 137, 138, 139, 140].

In this section we examine a single-mode THz microcavity [141, 142, 143, 144] with an embedded Aharonov-Bohm quantum ring, which is pierced by a magnetic flux and subjected to a lateral electric field. We restrict our analysis to linearly polarized microcavity radiation only. The geometry of the system is shown in Fig. 10. The emission properties of such a system under continuous incoherent pumping
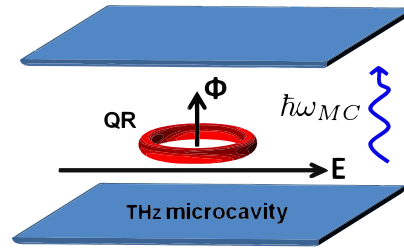
Fig. 10 An Aharonov-Bohm quantum ring embedded into a single-mode THz microcavity. (From Ref. [5]).

are studied theoretically. We calculate the luminescence spectrum of the system using the master equation techniques for several combinations of the applied external electric and magnetic fields. We demonstrate that the resonance which is best for exploring quantum features of the system [138] can be achieved by means of tuning the magnitude of the lateral electric field. An additional degree of control can be achieved by changing the angle between the polarization plane of the optical pump and the lateral electric field. As we show, the quantum ring-microcavity coupling strength depends strongly on the above mentioned angle.

5.2 Quantum rings in high-quality terahertz microcavities

5.2.1 Aharonov-Bohm quantum rings as two-level photon emitters

In this Section we briefly revise the energy spectrum and optical properties of a single-electron Aharonov-Bohm QR pierced by a magnetic flux Φ and subjected to a lateral electric field $\mathbf{E}$, which were studied in Section 4. We then show how the single-electron Aharonov-Bohm QR can be utilized as a two-level, single-photon emitter.

In the absence of the external electric field the eigenfunctions of an infinitely narrow Aharonov-Bohm QR of a radius R are given by

$$\psi_m(\varphi) = e^{im\varphi}/\sqrt{2\pi}, \tag{62}$$

where φ is the polar angle coordinate and $m = 0, \pm 1, \pm 2...$ is the angular momentum quantum number. The corresponding eigenvalues are defined by

$$\varepsilon_m(f) = \varepsilon_{QR}(m+f)^2,$$

where $\varepsilon_{QR} = \hbar^2/2M_e R^2$ is the energy scale of the interlevel separation in the QR, M_e is the electron effective mass and $f = \Phi/\Phi_0$ is the number of flux quanta piercing the QR ($\Phi_0 = h/e$). For experimentally attainable QRs, ε_{QR} corresponds to the THz frequency range.

When the lateral electric field is applied, the modified electron eigenfunctions can be expressed as a linear combination of the unperturbed wave functions (62):

$$\Psi_n(\varphi) = \sum_m c_m^n e^{im\varphi}. \tag{63}$$

Substituting the wave function (63) into the Schrödinger equation with the Hamiltonian containing a term which describes the presence of the lateral electric field, multiplying the resulting expression by $e^{-im\varphi}$, and integrating with respect to the angle φ results in an infinite system of linear equations for the coefficients c_m^n (for details see Section 4.2)

$$\left[(m+f)^2 - \lambda_n\right] c_m^n + \beta\left(c_{m+1}^n + c_{m-1}^n\right) = 0, \tag{64}$$

where $\beta = eER/2\varepsilon_{QR}$ is the normalized strength of the lateral electric field and λ_n is an energy eigenvalue normalized by ε_{QR}. It can be seen from the system of equations (64) that all the QR quantities are periodic in the magnetic flux Φ with the period equal to Φ_0. There is also an apparent symmetry with respect to the change of the sign of Φ. Therefore, in what follows we will consider only the case of $0 \leq \Phi \leq \Phi_0/2$.

It it shown in Appendix 6.2 that in the limit of a weak in-plane electric field, $eER \ll \varepsilon_{QR}$, all essential features of the first three states of the QR are fully captured by the following 3×3 system of linear equations:

$$\begin{pmatrix} (f+1)^2 & \beta & 0 \\ \beta & f^2 & \beta \\ 0 & \beta & (f-1)^2 \end{pmatrix} \begin{pmatrix} c_{+1}^n \\ c_0^n \\ c_{-1}^n \end{pmatrix} = \lambda_n \begin{pmatrix} c_{+1}^n \\ c_0^n \\ c_{-1}^n \end{pmatrix}. \tag{65}$$

In what follows we will be interested in the transitions between the ground and the first excited states in the QR only. However, in order to obtain accurate ground and first excited states eigenenergies and eigenfunctions all three listed states should be considered. The system of linear equations (65) can be reduced to a cubic equation for λ_n, which yields the following eigenvalues $\lambda_1 < \lambda_2 < \lambda_3$:

$$\lambda_1 = -2/3\sqrt{1+12f^2+6\beta^2}\cos(\alpha/3)+f^2+2/3, \tag{66}$$

$$\lambda_2 = -2/3\sqrt{1+12f^2+6\beta^2}\cos(\alpha/3-2\pi/3)+f^2+2/3, \tag{67}$$

$$\lambda_3 = -2/3\sqrt{1+12f^2+6\beta^2}\cos(\alpha/3+2\pi/3)+f^2+2/3, \tag{68}$$

where

$$\cos\alpha = \frac{1-36f^2+9\beta^2}{(1+12f^2+6\beta^2)^{3/2}}.$$

The set of corresponding eigenvectors (non-normalized) is given by substituting appropriate values of λ_n into

$$\begin{pmatrix} c_{+1}^n \\ c_0^n \\ c_{-1}^n \end{pmatrix} = \begin{pmatrix} \left[\lambda_n - (f-1)^2\right]\left(\lambda_n - f^2\right) - \beta^2 \\ \left[\lambda_n - (f-1)^2\right]\beta \\ \beta^2 \end{pmatrix}. \tag{69}$$

The energy spectrum for the electron ground and the first excited states defined by Eq. (66) and Eq. (67) respectively for $\beta = 0.1$ and $0 \leq f \leq 1/2$ is plotted in Fig. 11. Notably, the 3×3 system of equations (65) provides a very good accuracy for the
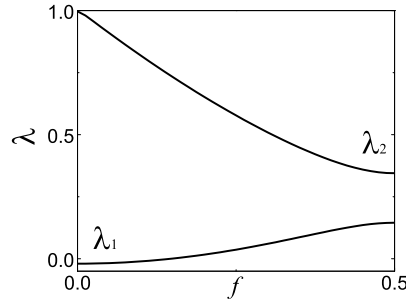
Fig. 11 The normalized energy spectrum for the electron ground and the first excited states in the quantum ring as a function of dimensionless parameter f for $\beta = 0.1$. (From Ref. [5]).

ground and the first excited states when $\beta \lesssim 1$ (i.e. $eER \lesssim \varepsilon_{QR}$). A numerical check

shows that the further increase in the system of linear equations, Eq. (64), does not provide any noticeable change in the results. A similar analysis is applicable to a nanohelix with an electric field applied normal to its axis. For a helix, the role of magnetic flux in the absence of a magnetic field is played by the electron momentum along the helical line [112, 145, 113, 114].

The QR can be represented as a two-level system with the energy gap between the ground state $|g\rangle$ ($n = 1$) and the excited state $|e\rangle$ ($n = 2$) denoted by Δ. From Eqs. (66)–(67), it is clear that Δ depends on both the external electric field $\mathbf{E}$, applied in the QR plane, and the magnetic flux Φ, piercing the QR. In particular, when $\Phi = 0$ ($\Phi = \Phi_0/2$), one obtains $\Delta/\varepsilon_{QR} = 1 + 2\beta^2$ ($\Delta/\varepsilon_{QR} = 2\beta$).

Another quantity, which is needed for further calculations, is the product of the light polarization vector $\mathbf{e}$ and the matrix element $\mathbf{d} = \langle e|\hat{\mathbf{d}}|g\rangle = \langle g|\hat{\mathbf{d}}|e\rangle$ of the dipole moment calculated between the ground state $|g\rangle$ and the excited state $|e\rangle$. For linearly polarized light this product is given by the following integral:

$$\mathbf{d} \cdot \mathbf{e} = eR \int_0^{2\pi} \Psi_e \Psi_g \cos(\theta - \varphi)\, d\varphi, \tag{70}$$

where Ψ_g, Ψ_e are the ground and the first excited state wave functions defined by Eq. (63) and θ is the angle between $\mathbf{e}$ and $\mathbf{E}$.

Substituting eigenfunctions Ψ_g, Ψ_e given by Eq. (63) into Eq. (70) and performing the integration with respect to the angle φ we obtain

$$\mathbf{d} \cdot \mathbf{e} = \left(d_-^2 + d_+^2 - 2d_- d_+ \cos 2\theta\right)^{1/2}, \tag{71}$$

where

$$d_- = \frac{eR}{2}\left|c_0^e c_{-1}^g + c_{+1}^e c_0^g\right|, \tag{72}$$

and

$$d_+ = \frac{eR}{2}\left|c_{-1}^e c_0^g + c_0^e c_{+1}^g\right|. \tag{73}$$

Later in this work we use Eqs. (71)–(73) with coefficients c^e, c^g obtained from Eq. (69) to calculate the QR-MC coupling strength. A detailed analysis of Eq. (69) and Eqs. (72)–(73) shows that a noticeable θ-dependence in Eq. (71) occurs only when $f = 0$ or $f = 1/2$, as d_- vanishes otherwise.

5.2.2 The Jaynes-Cummings Hamiltonian and the Master Equation

The full Hamiltonian describing the system of a QR coupled to a single-mode THz MC is the Jaynes-Cummings [146][2]

$$H_{JC} = \Delta \sigma^\dagger \sigma + \hbar \omega_{MC} a^\dagger a + \mathscr{G}\left(\sigma^\dagger a + \sigma a^\dagger\right), \tag{74}$$

---

[2] For more details on MC-2LE interaction Hamiltonian, i.e. the Jaynes-Cummings Hamiltonian, please refer to Sections 3.2.1-3.2.3 of this chapter.

where ω_{MC} is the MC eigenfrequency, $\mathscr{G}$ is the QR-MC coupling constant, $a^\dagger$ is the MC photon creation operator, a is the MC photon annihilation operator, $\sigma^\dagger = (\sigma_x + i\sigma_y)/2$ is the QR electron creation operator, $\sigma = (\sigma_x - i\sigma_y)/2$ is the QR electron annihilation operator, and σ_x, σ_y are the Pauli matrices acting in the space of $|g\rangle$ and $|e\rangle$ states. The frequency of the MC mode and the frequency of the transition between the QR states are assumed to be close enough to allow the use of the rotating wave approximation. [147, 148] If the MC mode is linearly polarized, $\mathscr{G}$ is given by

$$\mathscr{G} = -\left(\mathbf{d}\cdot\mathbf{e}\right)\sqrt{\hbar\omega_{MC}/2\varepsilon_0 V}, \tag{75}$$

where $\mathbf{d}\cdot\mathbf{e}$ is given by Eq. (71), ε_0 is the vacuum dielectric permittivity, V is the quantization volume, which can be estimated as $V \approx (\lambda_{MC}/2)^3$, and $\lambda_{MC} = 2\pi c/\omega_{MC}$ is the MC characteristic wavelength. When the magnetic flux piercing the QR is equal to an integer number of half-flux quanta, $\mathscr{G}$ strongly depends on the angle θ between the projection of the radiation polarization vector onto the QR plane and the applied lateral electric field.

The eigenvalues of the Hamiltonian (74) are the same as in the case of a single-mode MC with embedded QD, whose excitations obey fermionic statistics [138, 147].

$$E_N^\pm = \hbar\omega_{MC}(N-1/2) + \Delta/2 \pm \sqrt{(\hbar\omega_{MC}-\Delta)^2/4 + N\mathscr{G}^2}, \tag{76}$$

where N is the total number of electron-photon excitations in the system, i.e. the number of photons inside the MC if the electron is in the ground state. The corresponding eigenfunctions $\mathscr{X}_N^\pm$ can be expressed as a linear combination of the combined electron-photon states $|g,N\rangle = |g\rangle \otimes |N\rangle$ and $|e,N-1\rangle = |e\rangle \otimes |N-1\rangle$, which define both the QR state and the MC photon occupation number. Using this basis we solve a 2×2 system of linear equations which corresponds to the Hamiltonian (74) and obtain

$$\mathscr{X}_N^\pm = K_{g,N}^\pm |g,N\rangle + K_{e,N}^\pm |e,N-1\rangle, \tag{77}$$

where

$$K_{g,N}^\pm = \frac{\sqrt{N}\mathscr{G}}{\sqrt{\left(E_N^\pm - N\hbar\omega_{MC}\right)^2 + N\mathscr{G}^2}}, \tag{78}$$

and

$$K_{e,N}^\pm = \frac{E_N^\pm - N\hbar\omega_{MC}}{\sqrt{\left(E_N^\pm - N\hbar\omega_{MC}\right)^2 + N\hbar\mathscr{G}^2}}. \tag{79}$$

The main advantage of using a QR instead of a QD is the opportunity to control both the energy gap Δ between the first two states of the QR and the QR-MC coupling constant $\mathscr{G}$ by changing the external electric and magnetic fields. These fields can be used to achieve the resonant condition $\Delta = \hbar\omega_{MC}$ and provide easy means of performing a transition from the strong to the weak coupling regime within the same system [138].

The eigenvalues $E_N^\pm$ defined by Eq. (76) form the so-called "Jaynes-Cummings ladder" and the emission spectrum of the system, which is observed outside of

the MC, is defined by optical transitions between the states with total number of electron-photon excitations N different by unity (see Fig. 12). Inside a non-ideal
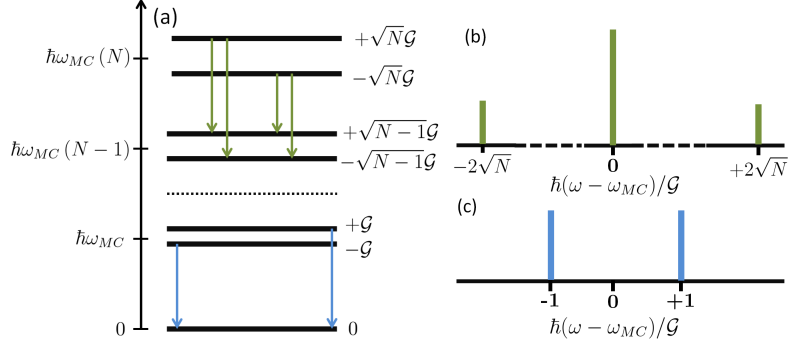
Fig. 12 Schematic diagram of the energy and emission spectra of the coupled QR-MC system in the resonant case $\Delta = \hbar\omega_{MC}$: (a) the "Jaynes-Cummings ladder"; (b) the Mollow triplet; (c) the Rabi doublet.

MC, a photon has a limited lifetime and when the photon leaks out, one can measure its frequency. This provides a direct access to the quantized coupled electron-photon states of the system.

In order to describe any realistic experiment measuring the QR-MC emission spectrum one should introduce pump and decay in the system. We model the system dynamics under incoherent MC pumping and account for dissipation processes using the master equation approach for the full density matrix of the system ρ (see, e.g., Refs. [147, 148])[3]. The master equation reads

$$\frac{\partial \rho}{\partial t} = \frac{i}{\hbar}[\rho, H_{JC}] + \mathscr{L}_P^{MC}\rho + \mathscr{L}_\gamma^{MC}\rho + \mathscr{L}_\gamma^{QR}\rho, \qquad (80)$$

where $\mathscr{L}_P^{MC}$, $\mathscr{L}_\gamma^{MC}$ are the Lindblad terms, which account for the MC pump and decay, and the Lindblad term $\mathscr{L}_\gamma^{QR}$ describes non-radiative transitions of the QR electron from the excited state $|e\rangle$ to the ground state $|g\rangle$. In the explicit form these three terms are given by

$$\mathscr{L}_P^{MC}\rho = \frac{P_{MC}}{2}(2a^\dagger\rho a - aa^\dagger\rho - \rho aa^\dagger + 2a\rho a^\dagger - a^\dagger a\rho - \rho a^\dagger a),$$

$$\mathscr{L}_\gamma^{MC}\rho = \frac{\gamma_{MC}}{2}(2a\rho a^\dagger - a^\dagger a\rho - \rho a^\dagger a),$$

$$\mathscr{L}_\gamma^{QR}\rho = \frac{\gamma_{QR}}{2}(2\sigma\rho\sigma^\dagger - \sigma^\dagger\sigma\rho - \rho\sigma^\dagger\sigma),$$

---

[3] For more details on the master equation approach for the full density matrix of a general MC-2LE system please see Sections 3.2.4-3.2.5 of this chapter.

where P_{MC} is the intensity of the incoherent MC pumping and γ_{MC}, γ_{QR} are the lifetimes of the photonic and the QR excitations respectively. Due to the balance between the pump and the decay, after some time a steady state is established. We denote the corresponding density matrix as ρ^{SS}. The steady state density matrix can be found by solving numerically Eq. (80) with all the matrices truncated. When performing the truncation, all the states which can be excited as a result of the pumping should be accounted for.

5.2.3 Emission spectrum of the system under incoherent pumping

In the presence of the pump and the decay and after establishing an equilibrium, the system is in a mixed state, which is characterized by the full density matrix ρ^{SS}. If ρ^{SS} is written in the basis of eigenfunctions (77), the density matrix diagonal element ρ_{II}^{SS} gives the probability of the system to be in the Ith state. At low pumping, $P_{MC} \ll \mathscr{G}$, and in the case of a high-Q system, $\gamma_{MC}, \gamma_{QR} \ll \mathscr{G}$, which is the best regime to elucidate quantum coupling effects [138], the emission spectrum can be calculated using the so-called manifold method, which has been proved to provide qualitatively accurate results avoiding heavy numerical calculations (see, e.g., Refs. [138, 140], and [149]). In this approximation the QR and MC emission spectra are given by

$$S_{QR}(\omega) \approx \frac{1}{\pi} \sum_{I,F} \frac{\left| M_{IF}^{QR} \right|^2 \rho_{II}^{SS} \Gamma_{IF}}{\left(\hbar\Omega_{IF} - \hbar\omega \right)^2 + \Gamma_{IF}^2}, \tag{81}$$

$$S_{MC}(\omega) \approx \frac{1}{\pi} \sum_{I,F} \frac{\left| M_{IF}^{MC} \right|^2 \rho_{II}^{SS} \Gamma_{IF}}{\left(\hbar\Omega_{IF} - \hbar\omega \right)^2 + \Gamma_{IF}^2}, \tag{82}$$

where $\left| M_{IF}^{QR} \right|^2 = |\langle \mathscr{X}_F, | \sigma | \mathscr{X}_I \rangle|^2$, $\left| M_{IF}^{MC} \right|^2 = |\langle \mathscr{X}_F |a| \mathscr{X}_I \rangle|^2$, $\hbar\Omega_{IF} = E^I - E^F$, $\mathscr{X}_i$ and $\mathscr{X}_f$ are the QR-MC initial and final states eigenfunctions defined by Eq. (77), E^i and E^f are the QR-MC initial and final states eigenenergies defined by Eq. (76), and Γ_{IF} is given by

$$\Gamma_{IF} = \frac{\gamma_{QR}}{2} \sum_J \left(|M_{JI}^{QR}|^2 + |M_{JF}^{QR}|^2 \right) + \frac{\gamma_{MC}}{2} \sum_J \left(|M_{JI}^{MC}|^2 + |M_{JF}^{MC}|^2 \right)$$
$$+ \frac{P_{MC}}{2} \sum_J \left(|M_{JI}^{MC}|^2 + |M_{JF}^{MC}|^2 + |M_{IJ}^{MC}|^2 + |M_{FJ}^{MC}|^2 \right).$$

In Eqs. (81)-(82) S_{QR} and S_{MC} correspond to photons of two different origins, which can be detected outside of the MC by an external observer: the direct emission of the QR and the leaking MC photons. In the first case a photon outside of the MC is created as a result of the QR electron transition from the excited state $|e\rangle$ to the ground state $|g\rangle$ and in the second case the photon is created due to annihilation of a MC photon. Substituting $\mathscr{X}_N^{\pm}$ from Eq. (77) into the expressions for $\left| M_{IF} \right|^2$ yields

$$\left|M_{IF}^{QR}\right|^2 = \left|K_{g,N_F}^{\pm} K_{e,N_I}^{\pm}\right|^2 \delta_{N_F,N_I-1},$$

$$\left|M_{IF}^{MC}\right|^2 = \left|\sqrt{N_I}K_{g,N_F}^{\pm} K_{g,N_I}^{\pm} + \sqrt{N_F}K_{e,N_F}^{\pm} K_{e,N_I}^{\pm}\right|^2 \delta_{N_F,N_I-1}.$$

It should be noted that only the transitions between the coupled electron-photon states with the total number of excitations differing by unity are allowed.

In the resonant case $\Delta = \omega_{MC}$, for transitions from the Nth state to the $(N-1)$th state we obtain

$$\left|M_{\pm \to \mp}^{QR}\right|^2 = 1/4, \tag{83}$$

$$\left|M_{\pm \to \pm}^{QR}\right|^2 = 1/4, \tag{84}$$

and

$$\left|M_{\pm \to \mp}^{MC}\right|^2 = \left|\sqrt{N} - \sqrt{N-1}\right|^2 /4, \tag{85}$$

$$\left|M_{\pm \to \pm}^{MC}\right|^2 = \left|\sqrt{N} + \sqrt{N-1}\right|^2 /4, \tag{86}$$

with corresponding eigenfrequencies given by

$$\Omega_{\pm \to \mp} = \omega_{MC} \pm \mathscr{G}\left(\sqrt{N} + \sqrt{N-1}\right)/\hbar, \tag{87}$$

$$\Omega_{\pm \to \pm} = \omega_{MC} \pm \mathscr{G}\left(\sqrt{N} - \sqrt{N-1}\right)/\hbar. \tag{88}$$

One can see that the observed emission spectrum consists of two symmetric inner peaks at frequencies (88) and two symmetric outer peaks at frequencies (87). Together, these peaks form the so-called "Jaynes-Cummings fork". From Eqs. (83)–(86) it follows that when the total number of electron-photon excitations in the initial state $N = 1$, both S_{QR} and S_{MC} have a shape of the Rabi doublet (see Fig. 12 (c)), and in the case of large excitation numbers, $N \gg 1$, S_{QR} is in the form of the Mollow triplet (see Fig. 12 (b)) while S_{MC} collapses into a single lasing peak.

5.3 Results and discussion

In this section we use the formalism which was developed in the previous Sections to calculate emission spectra of the QR-MC system in the presence of a magnetic flux Φ piercing the QR and a lateral electric field $\mathbf{E}$. The QR-MC system has apparent advantages for exploring the quantum nature of light-matter coupling in nanostructured systems compared to the well-studied QD-based setup. Namely, the parameters of the system can be more easily tuned by external fields. Between all possible combinations of the applied magnetic and electric fields there are two cases of considerable interest: (a) $\Phi = 0$, $\mathbf{e} \perp \mathbf{E}$ and (b) $\Phi = \Phi_0/2$, $\mathbf{e} \perp \mathbf{E}$. In both cases, the energy gap between the QR states is tunable by the strength of the lateral elec-

tric field. From Eqs. (66)–(67) we get $\Delta/\varepsilon_{QR} = 1 - 2\beta^2$ ($\Delta/\varepsilon_{QR} = 2\beta$) for $\Phi = 0$ ($\Phi = \Phi_0/2$). Thus, the energy gap Δ can be easily adjusted to coincide with the energy of the MC mode $\hbar\omega_{MC}$. From Eqs. (71)–(73) and Eq. (75) one can see that when $\Phi = 0$ or $\Phi = \Phi_0/2$ the QR-MC coupling constant $\mathscr{G}$ strongly depends on the angle θ between the direction of the external electric field and the projection of the MC mode polarization vector onto the QR plane. If $\mathbf{e} \perp \mathbf{E}$, the coupling constant $\mathscr{G}$ reaches its maximum possible value, and if $\mathbf{e} \parallel \mathbf{E}$, the MC mode and the QR are completely uncoupled. By changing the direction of the lateral electric field one acquires additional means of control of the emission spectrum of the system.

The quantum structure of the Jaynes-Cummings states discussed in the previous Section is known to be observed only in the low dissipation regime [138]. Therefore, it is natural to consider a QR embedded into a high-Q THz MC under a weak incoherent pumping. Similar to Ref. [138], we choose a MC with the decay rate $\gamma_{MC}/\mathscr{G} = 0.1$ and a QR with the decay rate $\gamma_{QR}/\mathscr{G} = 0.01$. The QR decay rate is chosen to be much smaller than the MC decay rate, as is the case in most experimental systems [80, 82]. In all the calculations we chose either $P_{MC}/\mathscr{G} = 0.005$ or $P_{MC}/\mathscr{G} = 0.095$. These conditions satisfy the applicability criteria of the manifold method for modelling the emission spectrum of the systems.

In order to estimate experimental conditions for the observation of the predicted emission spectra we use the following values of the other system parameters: a typical radius of experimentally attainable [9, 10, 17] QRs, $R = 20$nm and the electron effective mass $M = 0.05m_e$. This gives the energy scale of the QR interlevel separation $\varepsilon_{QR} \simeq 2$meV and the magnitude of the magnetic field, which produces a magnetic flux through the QR equal to a half of the flux quantum, $B \simeq 2$T. Unless specified otherwise, all the calculations are made in the presence of a weak lateral electric field $\mathbf{E} \perp \mathbf{e}$ with the magnitude $E = 0.1\varepsilon_{QR}/eR = 2 \cdot 10^4$V/m. The QR-MC coupling constant can now be estimated using Eq. (75). we obtain $\mathscr{G} = 8.3 \cdot 10^{-4}$meV ($\mathscr{G} = 1.2 \cdot 10^{-3}$meV) for $\Phi = 0$ ($\Phi = \Phi_0/2$) which results in the MC Q-factor requirement $Q = \hbar\omega_{MC}/\gamma_{MC} \approx 16000$ ($Q \approx 5000$). THz microcavities with the Q-factor of this order of magnitude have already been achieved [142].

We start with calculations of the emission spectrum of the system for $P_{MC}/\mathscr{G} = 0.005$ and $P_{MC}/\mathscr{G} = 0.095$ in the resonant case, $\hbar\omega_{MC} = \Delta$. The magnetic flux piercing the QR is either $\Phi = 0$ or $\Phi = \Phi_0/2$. Results of these calculations are shown in Fig. 13. Both the direct QR emission spectrum, S_{QR}, and the MC emission spectrum S_{MC} are plotted. When $P_{MC}/\mathscr{G} = 0.005$, there are two dominant peaks (the linear Rabi doublet) in S_{QR} and S_{MC} at the frequencies $\omega = \pm\mathscr{G}/\hbar$, which correspond to the transitions between the two $N = 1$ states and the ground $N = 0$ state. With increasing pumping, $P_{MC}/\mathscr{G} = 0.095$, the higher, $N > 1$, states are excited. The intensity of the Rabi doublet is decreased while the quadruplet peaks corresponding to the transitions between the $N = 2$ and $N = 1$ states emerge. Only the inner quadruplet peaks in S_{QR} and S_{MC} can be seen in the selected energy range. It should be mentioned that the outer peaks in the MC emission spectrum, S_{MC}, become suppressed with increasing N, as can be seen from the expression for the corresponding matrix elements, Eq. (85).
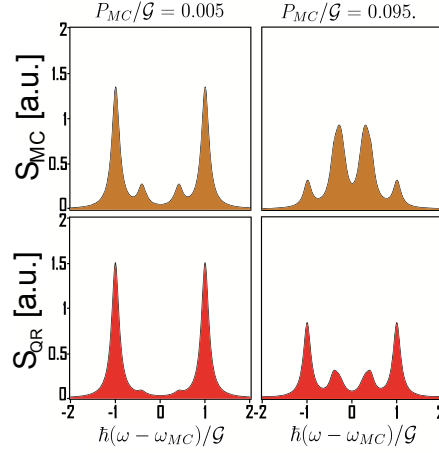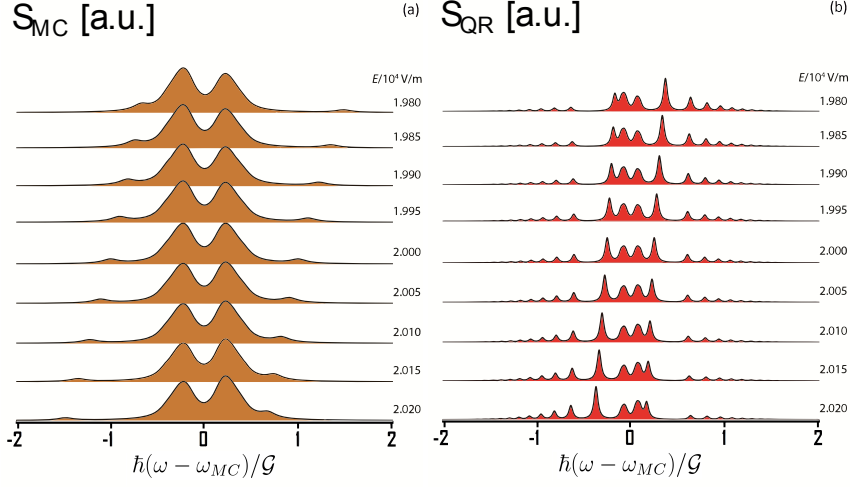
Fig. 13 Emission spectrum of the quantum ring-microcavity system in the presence of a lateral electric field $E = 2.00 \times 10^4 \, \text{V/m}$ for $P_{MC}/\mathscr{G} = 0.005$ and $P_{MC}/\mathscr{G} = 0.095$. The microcavity mode is in resonance with the quantum ring transition. The upper row (brown) corresponds to the microcavity emission and the lower row (red) corresponds to the direct quantum ring emission. The magnetic flux piercing the quantum ring is either $\Phi = 0$ or $\Phi = \Phi_0/2$. The emission frequencies are normalized by the quantum ring-microcavity coupling constant $\mathscr{G}/\hbar$ and centred around ω_{MC}. (From Ref. [5]).

A different type of emission spectrum can be observed away from the resonance. This can be achieved for the same system by changing the magnitude of the lateral electric field. In Figs. 14–15 we plot S_{MC} and S_{QR} when $\Delta \neq \hbar\omega_{MC}$ for several values of E. Fig. 14 corresponds to $\Phi = 0$, whereas Fig. 15 corresponds to $\Phi = \Phi_0/2$. Due to the fact that there are non-zero probabilities of finding the system in states with different N, the emission spectrum has a pronounced multiplet structure. The MC pumping rate is taken as $P_{MC}/\mathscr{G} = 0.095$. One can clearly see the avoided crossings in the plotted emission spectra, manifesting that the system is in the strong coupling regime. When $\Phi = \Phi_0/2$ and the detuning between Δ and $\hbar\omega_{MC}$ is of the order of $\mathscr{G}$, the direct QR emission spectrum has the most intensive peaks at the frequencies close to $\omega = \Delta/\hbar$. This indicates that the QR is almost uncoupled from the MC. The more pronounced changes in the emission

spectra in Fig. 15 compared to Fig. 14 can be explained by different dependences of the energy gap Δ on the magnitude of the lateral electric field E: when $\Phi = \Phi_0/2$ the dependence is linear in E and when $\Phi = 0$ the dependence is quadratic in E.

For a nearly zero flux through the QR, a small change of the flux results in significant changes in S_{MC} and S_{QR}, as the presence of a weak magnetic field affects strongly both the QR gap Δ and the QR-MC coupling constant $\mathscr{G}$. The dependence of the QR gap Δ on the magnetic flux Φ piercing the QR can be seen from Fig. 11, while the QR-MC coupling constant $\mathscr{G}$ magnetic flux dependence can be easily calculated using Eqs. (71)–(73) and Eq. (75). In Fig. 16 we plot S_{MC} and S_{QR} for several values of Φ near zero. The MC pumping rate is taken as $P_{MC}/\mathscr{G}_0 = 0.095$, where
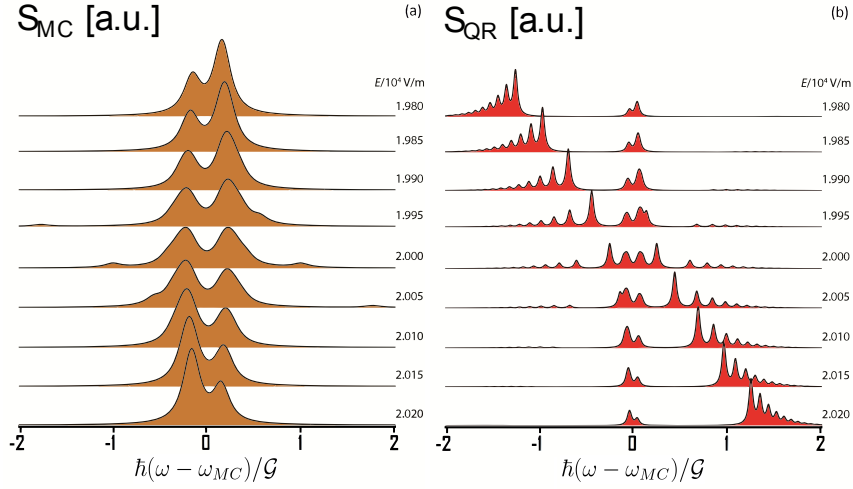
Fig. 14 Anticrossing in the emission spectrum of the quantum ring-microcavity system at various magnitudes of the external lateral electric field E from $1.98 \times 10^4 \text{V/m}$ to $2.02 \times 10^4 \text{V/m}$ with the increment 50V/m: (a) microcavity emission spectrum (brown), (b) direct quantum ring emission spectrum (red). The magnetic flux piercing the quantum ring $\Phi = 0$. The resonance case $\Delta = \hbar\omega_{MC}$ corresponds to $E = 2.00 \times 10^4 \text{V/m}$. The microcavity pumping rate $P_{MC}/\mathcal{G} = 0.095$. The emission frequencies are normalized by the quantum ring-microcavity coupling constant $\mathcal{G}/\hbar$ and centred around ω_{MC}. (From Ref. [5]).

$\mathcal{G}_0$ denotes the value of the QR-MC coupling constant for $\Phi = 0$. The plotted emission spectra incorporate both the anticrossing behaviour due to detuning of the QR transition energy from the energy of the MC mode and the changes in the multiplet structure owing to varying the QR-MC coupling strength.

Finally, we calculate the emission spectrum of the QR-microcavity system altering the angle θ between the direction of the applied electric field and the projection of the microcavity mode polarization vector onto the QR plane. Again, the magnetic flux piercing the QR is either $\Phi = 0$ or $\Phi = \Phi_0/2$. The system is in the resonance, $\Delta = \hbar\omega_{MC}$. The microcavity pumping rate is taken as $P_{MC}/\mathcal{G}_{\pi/2} = 0.005$, where $\mathcal{G}_{\pi/2}$ denotes the value of the QR-microcavity coupling constant for $\theta = \pi/2$. The results are plotted in Fig. 17. One can see that as the angle θ is changed, the emission peaks shift towards the microcavity eigenfrequency ω_{MC}, which can be explained by reducing the coupling strength $\mathcal{G}$. This effect provides an additional way to control the frequency of the satellite peaks in the QR-microcavity emission spectrum and allows a purely spectroscopic measurement of the pump polarization.

In this work we dealt exclusively with the QR inter-subband transitions. However, a similar analysis should be possible for inter-band optical transitions, for which matrix elements and energies can also be tuned by the external fields more easily than in the widely studied QD systems.
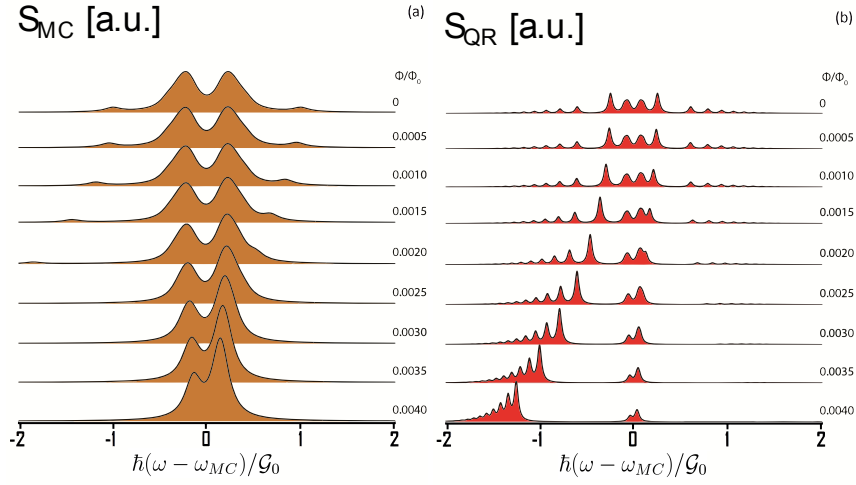
Fig. 15 Anticrossing in the emission spectrum of the quantum ring-microcavity system at various magnitudes of the external lateral electric field E from $1.98 \times 10^4 \text{V/m}$ to $2.02 \times 10^4 \text{V/m}$ with the increment 50V/m: (a) microcavity emission spectrum (brown), (b) direct quantum ring emission spectrum (red). The magnetic flux piercing the quantum ring $\Phi = \Phi_0/2$. The resonance case $\Delta = \hbar \omega_{MC}$ corresponds to $E = 2.00 \times 10^4 \text{V/m}$. The microcavity pumping rate $P_{MC}/\mathscr{G} = 0.095$. The emission frequencies are normalized by the quantum ring-microcavity coupling constant $\mathscr{G}/\hbar$ and centred around ω_{MC}. (From Ref. [5]).

In conclusion, we have analyzed the emission spectrum of an Aharonov-Bohm QR placed into a single-mode quantum MC. We have shown that the emission spectrum in the strong coupling regime has a multiplet structure and can be tuned by the variation of the magnetic field piercing the QR and by changing the strength and direction of the applied lateral electric field. Thus, it is demonstrated that a MC with an embedded QR is a promising system for use as a tunable optical modulator in the THz range. The QR-MC system, which allows manipulation of quantum states with external fields, might also prove to be useful for investigating dephasing mechanisms and for engineering and exploring enhanced light-matter interactions for novel quantum investigations.

6 Conclusions and outlook. Bridging the THz gap with Aharonov-Bohm quantum rings.

6.1 Conclusions

In our work we studied the interaction of Aharonov-Bohm quantum rings with classical and quantized electromagnetic fields.

Fig. 16 Anticrossing in the emission spectrum of the quantum ring-microcavity system at various magnitudes of the magnetic flux Φ piercing the quantum ring from 0 to $0.004\Phi_0$ with the increment $5 \times 10^{-4}\Phi_0$ and in the presence of the lateral electric field $E = 2.00 \times 10^4 \text{V/m}$: (a) microcavity emission spectrum (brown), (b) direct quantum ring emission spectrum (red). The resonance case $\Delta = \hbar\omega_{MC}$ corresponds to $\Phi = 0$. The emission frequencies are normalized by the value of the quantum ring-microcavity coupling constant calculated for $\Phi = 0$ ($\mathscr{G}_0$) and centred around ω_{MC}. The microcavity pumping rate $P_{MC}/\mathscr{G}_0 = 0.095$. (From Ref. [5]).

In Section 4 we examined an infinitely-narrow, single-particle quantum ring pierced by a magnetic flux and subjected to a static lateral electric field [3, 2]. This model is relevant to nanoscale-sized type-I quantum rings and type-II quantum dots, such as those studied in Refs. [6, 7, 8, 9, 10, 11, 12, 13, 14, 15, 16, 17, 18, 19, 20, 21, 22, 23, 24, 25, 26, 27, 28, 29, 30, 31, 32]. We show that the applied electric field, which is known to suppress magneto-oscillations in the ground state of a single-particle quantum ring [110, 111], results in strong oscillations of the ring electric dipole moment and selection rules for optical transitions between the ground and first excited states of the quantum ring. We attribute these phenomena to electric-field induced mixing of quantum ring states with different angular momenta, which occurs when magnetic flux through the quantum ring is equal to a half-integer of the magnetic flux quantum. It is shown that even a weak electric field causes this mixing. Most of the results obtained here for the static in-plane electric field can be easily generalized to the case of the rotating field by a proper change of the coordinates system [4].

It should be also emphasised that calculated effects are not an artifice of the infinitely-narrow ring model used in our calculations, but persist in finite-width rings in a uniform magnetic field. As we have shown, the only feature needed for the discussed phenomena is the degeneracy of the states with the angular momenta
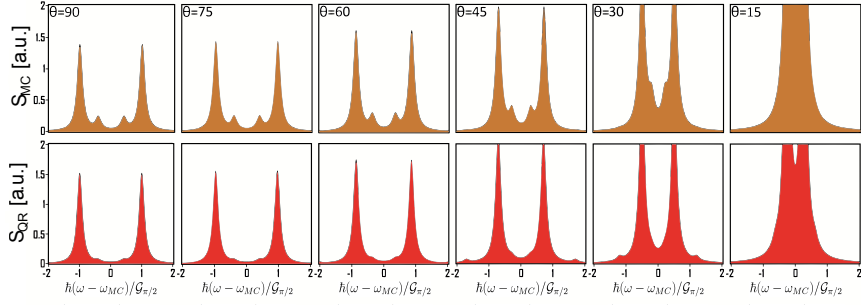
Fig. 17 Emission spectrum of the quantum ring-microcavity system when the lateral electric field $E = 2.00 \times 10^4 \text{V/m}$ is rotated. The angle θ is counted between $\mathbf{E}$ and the projection of the microcavity mode polarization vector onto the quantum ring plane $\mathbf{e}$. The upper row (brown) corresponds to the microcavity emission and the lower row (red) correspond to the direct quantum ring emission. The system is in resonance, $\Delta = \hbar\omega_{MC}$. The emission frequencies are normalized by the value of the quantum ring-microcavity coupling constant for $\theta = \pi/2$ ($\mathscr{G}_{\pi/2}$) and centred around ω_{MC}. The microcavity pumping rate $P_{MC}/\mathscr{G}_{\pi/2} = 0.095$. (From Ref. [5]).

differing by one at certain magnetic field values, which is known to be present in quantum rings of finite width [57, 58, 59, 60, 115].

In order to establish an understanding of the potential for observation of the predicted effects in real systems we provide estimates for experimental conditions essential for measuring these phenomena. While observation of the dipole moment magneto-oscillations would require a low-temperature laboratory, the oscillations of selection rules for optical transitions can be potentially observed at room temperatures. Indeed, when the ground and the first excited stated are equally occupied the dipole moment oscillations are completely suppressed while the intensity of the optical transitions is only four times lower comparing to the case when the ground state is fully occupied and the first excited state is empty.

For experimentally attainable quantum rings these transitions occur in the THz frequency range. It provides an opportunity of utilizing Aharonov-Bohm quantum rings as THz emitters and detectors. Despite significant progress made towards reliable and efficient THz sources, such as THz quantum cascade lasers [150, 151, 152], free electron THz lasers [153, 154], and recently proposed microcavity-polaritons THz lasers [130, 132, 122, 123], bridging of the so-called 'THz gap' remains a formidable task. The range of potential application of THz radiation is both vast and in high demand. The vibrational modes of many molecules, including molecules of explosive materials, occur at THz frequencies [155, 156], making THz spectroscopy a powerful and non-invasive tool for molecular identification and characterization. An airport scanner, which detects molecules found in explosives is only one example of a highly-useful THz device. Other potential applications of the THz spectroscopy lie in the area of pharmaceutical research and biomedical diagnostics [157].

Arguably, the use of Aharonov-Bohm quantum rings for THz radiation and detection has its merits as polarization properties and frequencies of THz transitions in quantum rings are fully controlled by the applied external fields.

In Section 5 we examined a system of an Aharonov-Bohm quantum ring embedded into a single-mode THz microcavity [5]. It was shown that the discussed possibility to control optical properties of quantum rings with the external electric and magnetic fields suggests a new way of regulating the microcavity-emitter coupling strength. Such easy control was never possible with quantum dots embedded in microcavities where all main optical properties of the system are predefined at the growth stage. As a result, one can strongly influence emission spectra of the system by varying external fields.

We calculate the emission spectra of the system under continuous incoherent pumping when the quantum ring transitions are both in or out of the resonance with the microcavity mode and for various combinations of the applied electric and magnetic fields. We restrict our analysis to linearly polarized microcavity radiation only. It is shown that when the system is in resonance and the magnetic flux piercing the quantum ring is equal to a half-integer of the magnetic flux quantum, a precise control of the satellite peaks in the emission spectra is possible with (i) pumping intensity and (ii) the direction of the lateral electric field with respect to the microcavity radiation polarization vector. This effect can be used for creating the highly demanded THz electro-optical modulators. In a quantum ring-microcavity-based optical modulator, modulation of the intensity, frequencies and polarization of the THz radiation would be realized by periodic variation of the lateral electric field direction. Potentially, such a device can be indeed created as THz microcavities with high values of Q-factor based on both Bragg mirrors [158] and photonic crystals [142] have been already achieved.

The calculated non-resonant emission spectra can be of a great help during the procedure of modulator adjustment. As we discuss in Section 5, in order to establish a resonance in the quantum ring-microcavity system one would tune magnitudes of the applied electric and magnetic fields. Thus, the calculated non-resonant emission spectra can serve as a reference pattern.

To conclude, we believe Aharonov-Bohm quantum rings to be promising candidates for creating optical devices operating with radiation at THz frequencies and hope that our work will stimulate further experimental research in this area.

6.2 Outlook

A natural extension of the current work presented in Section 4 is to repeat our calculations using a more realistic (and consequently more complicated) 2D model of the Aharonov-Bohm quantum ring. We chose the same model as was utilized in Refs. [57, 58, 59, 60] as it allows an analytical treatment. Preliminary results of our calculations are shown in Fig. (18). One can see that, as it was stated, the main feature required for the predicted effects - degeneracy of the energy levels with angular

momenta differing by unity at certain magnetic field values - is indeed present in this model.
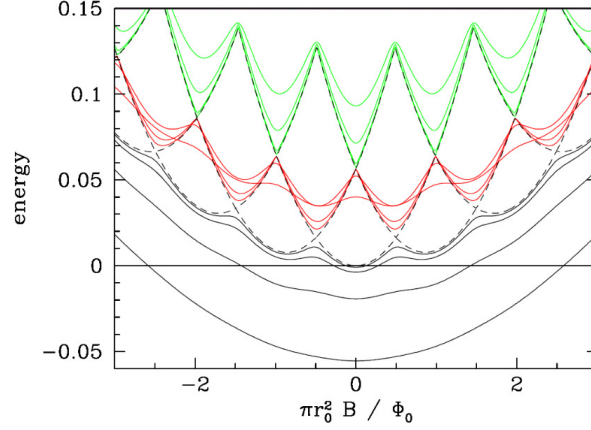
Fig. 18 A finite-width ring in a magnetic field for different values of in-plane electric field strength. The ring radius $r_0 = 100$nm and its width is 20nm.

The possible extension of the work presented in Section 5 is to use the quantum regression theorem [159, 92, 93, 147, 94] (together with the Wiener-Khintchine formula [160, 161, 92, 93, 147, 94]) to calculate the emission spectrum of the quantum ring-microcavity system. Such an approach can potentially reveal non-Lorentzian emission lineshapes.

Appendix. Analytical solutions for small matrices.

In the limit of weak electric field, $\beta = eER/(\hbar^2/M_e R^2) \ll 1$, the electron ground, first and second excited states are well-described by the following three-by-three system, which is obtained from Eq. (54) for $|m| \leq 1$

$$\begin{pmatrix} (f+1)^2 & \beta & 0 \\ \beta & f^2 & \beta \\ 0 & \beta & (f-1)^2 \end{pmatrix} \begin{pmatrix} c_{+1}^n \\ c_0^n \\ c_{-1}^n \end{pmatrix} = \lambda_n \begin{pmatrix} c_{+1}^n \\ c_0^n \\ c_{-1}^n \end{pmatrix}. \tag{89}$$

Here $f = (\Phi - N\Phi_0)/\Phi_0$ with N integer, so that $0 \leq f \leq 1/2$. The eigenvalues λ_n of the system (89) are the roots of the cubic equation

$$\lambda_n^3 - \lambda_n^2 \left(3f^2 + 2\right) + \lambda_n \left(3f^4 + 1 - 2\beta^2\right) - f^6 + 2f^4 - f^2 + 2f^2\beta^2 + 2\beta^2 = 0. \tag{90}$$

Solving Eq. (90) we find

$$\lambda_1 = -2/3\sqrt{1+12f^2+6\beta^2}\cos(\alpha/3) + f^2 + 2/3, \tag{91}$$

$$\lambda_2 = -2/3\sqrt{1+12f^2+6\beta^2}\cos(\alpha/3 - 2\pi/3) + f^2 + 2/3, \tag{92}$$

$$\lambda_3 = -2/3\sqrt{1+12f^2+6\beta^2}\cos(\alpha/3 + 2\pi/3) + f^2 + 2/3, \tag{93}$$

with

$$\cos\alpha = \frac{1 - 36f^2 + 9\beta^2}{(1+12f^2+6\beta^2)^{3/2}}.$$

Considering $\beta \ll 1$ (the limit of weak electric field) we expand Eqs. (91-93) into Taylor series in f to obtain

$$\lambda_1 = f^2 - 2\beta^2 \sum_{n=0}^{\infty} (2f)^{2n} + O(\beta^4), \tag{94}$$

$$\lambda_2 = 1 + f^2 + \beta^2 \left[1 - \sum_{n=0}^{\infty} \frac{(-1)^n (2n)!}{(1-2n)(n!)^2} \left(\frac{f}{\beta^2}\right)^{2n} \right] + O(\beta^4), \tag{95}$$

$$\lambda_3 = 1 + f^2 + \beta^2 \left[1 + \sum_{n=0}^{\infty} \frac{(-1)^n (2n)!}{(1-2n)(n!)^2} \left(\frac{f}{\beta^2}\right)^{2n} \right] + O(\beta^4). \tag{96}$$

It can be shown that Eqs. (95,96) coincide with the results of the perturbation theory in eER for quasi-degenerate states[96] if the coupling to the states with $|m| > 1$ is neglected.

The energy spectrum given by Eqs. (91-93) is plotted in Fig. 19. It is nearly indistinguishable from the energy spectrum, which was obtained by numerical diagonalization of the 23×23 system in Section 4 for the same value of β. A small discrepancy between the plotted energy spectra is noticeable only for the first and second excited states. The energy spectrum obtained by numerical diagonalization of the 23×23 system is slightly shifted towards the smaller energies. This shift occurs because the considered 3×3 matrix does not take into account the coupling between the $m = \pm 1$ and $m = \pm 2$ states. For the infinite system and $f = 0$, perturbation theory up to the second order in β yields

$$\lambda_1 = -2\beta^2, \ \lambda_2 = 1 - \beta^2/3, \ \lambda_3 = 1 + 5\beta^2/3, \tag{97}$$

whereas from Eqs. (94-96) one gets

$$\lambda_1 = -2\beta^2, \ \lambda_2 = 1, \ \lambda_3 = 1 + 2\beta^2. \tag{98}$$

The λ_2 and λ_3 values in Eq. (97) differ from the values in Eq. (98) by $-\beta^2/3$ which corresponds to the repulsion between the $m = \pm 1$ and $m = \pm 2$ states calculated using the second order perturbation theory.
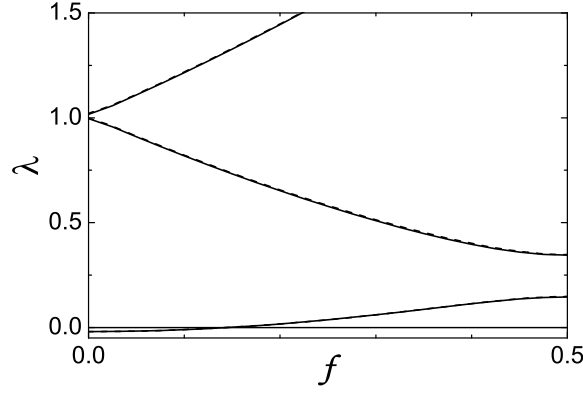
Fig. 19 The normalized energy spectrum as a function of dimensionless parameter f for $\beta = 0.1$. Dashed line - the result of analytical solution of the 3×3 system. Solid line - the result of numerical diagonalization of the 23×23 system. A horizontal line is shown to indicate $\lambda = 0$ value.

When $f = 1/2$, and in the absence of a lateral electric field, the $m = 0$ and $m = -1$ states are degenerate with energy $\varepsilon_1(0)/4$, i.e. $\lambda_1 = \lambda_2 = 1/4$, whereas the $m = +1$ state energy is nine times larger ($\lambda_3 = 9/4$). The contribution from this remote state can be neglected, and the electron ground and first excited states are well-described by the following two-by-two system, which contains c_{-1} and c_0 coefficients only,

$$\begin{pmatrix} f^2 & \beta \\ \beta & (f-1)^2 \end{pmatrix} \begin{pmatrix} c_0^n \\ c_{-1}^n \end{pmatrix} = \lambda_n \begin{pmatrix} c_0^n \\ c_{-1}^n \end{pmatrix}. \tag{99}$$

The eigenvalues λ_n of the system (99) are the roots of the quadratic equation

$$\lambda_n^2 - \lambda_n \left(2f^2 - 2f + 1 \right) + f^4 - 2f^3 + f^2 - \beta^2 = 0. \tag{100}$$

Solving Eq. (100) we find

$$\lambda_{1,2} = f^2 - f + 1/2 \mp \sqrt{f^2 - f + \beta^2 + 1/4}, \tag{101}$$

yielding for $f = 1/2$ the eigenvalue difference $\lambda_2 - \lambda_1 = 2\beta$, corresponding to the energy splitting of eER as expected from the perturbation theory for degenerate states. The energy spectrum given by Eq. (101) is plotted in Fig. 20 together with two lowest eigenvalues of the 23×23 system demonstrating a spectacular accuracy of the approximate solution for $\beta = 0.1$.

Let us now return to the three-by-three matrix and examine how its eigenvectors are modified with changing f. Near the point $f = 0$ it is convenient to write the eigenvectors of the system (89) in the following form
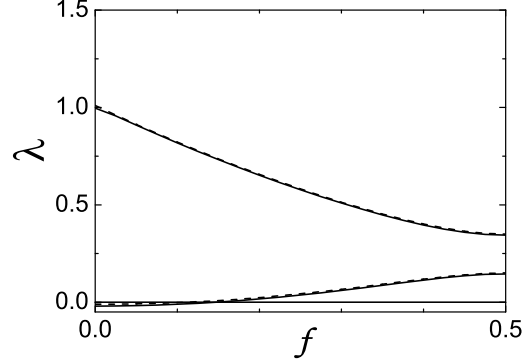
Fig. 20 The normalized energy spectrum as a function of dimensionless parameter f for $\beta = 0.1$. Dashed line - the result of analytical solution of the 2×2 system. Solid line - the result of numerical diagonalization of the 23×23 system. A horizontal line is shown to indicate $\lambda = 0$ value.

$$
\begin{pmatrix} c_{+1}^n \\ c_0^n \\ c_{-1}^n \end{pmatrix} = A_n \begin{pmatrix} \left[\lambda_n - (f-1)^2 \right] \left(\lambda_n - f^2 \right) - \beta^2 \\ \left[\lambda_n - (f-1)^2 \right] \beta \\ \beta^2 \end{pmatrix}, \qquad (102)
$$

where A_n denotes the normalization constant corresponding to the eigenvalue λ_n and (102) is valid only for $\beta \neq 0$. For $f = 0$ in the limit of weak electric field ($\beta \ll 1$) we obtain

$$
\begin{pmatrix} c_{+1}^1 \\ c_0^1 \\ c_{-1}^1 \end{pmatrix} = \frac{\left(1 + 1\sqrt{1 + 8\beta^2} + 8\beta^2 \right)^{-1/2}}{\sqrt{2}} \begin{pmatrix} -2\beta \\ 1 + \sqrt{1 + 8\beta^2} \\ -2\beta \end{pmatrix} \xrightarrow{\beta \to 0} \begin{pmatrix} 0 \\ 1 \\ 0 \end{pmatrix}, \quad (103)
$$

$$
\begin{pmatrix} c_{+1}^2 \\ c_0^2 \\ c_{-1}^2 \end{pmatrix} = \frac{1}{\sqrt{2}} \begin{pmatrix} -1 \\ 0 \\ 1 \end{pmatrix}, \qquad (104)
$$

$$
\begin{pmatrix} c_{+1}^3 \\ c_0^3 \\ c_{-1}^3 \end{pmatrix} = \frac{\left(1 - 1\sqrt{1 + 8\beta^2} + 8\beta^2 \right)^{-1/2}}{\sqrt{2}} \begin{pmatrix} 2\beta \\ \sqrt{1 + 8\beta^2} - 1 \\ 2\beta \end{pmatrix} \xrightarrow{\beta \to 0} \frac{1}{\sqrt{2}} \begin{pmatrix} 1 \\ 0 \\ 1 \end{pmatrix}. \quad (105)
$$

From Eqs. (103-105) one can see that for $f = 0$ and $\beta \ll 1$ the electron ground state is almost a pure $m = 0$ state, whereas the angular dependencies of the wavefunctions of the first and second excited states are well-described by $\sin \varphi$ and $\cos \varphi$ respectively.

The structure of eigenfunctions near $f = 1/2$ is best understood from Eq. (99), which yields

$$\begin{pmatrix} c_0^1 \\ c_{-1}^1 \end{pmatrix} = A \begin{pmatrix} \beta \\ 1/2 - f - \sqrt{f^2 - f + \beta^2 + 1/4} \end{pmatrix}, \tag{106}$$

$$\begin{pmatrix} c_0^2 \\ c_{-1}^2 \end{pmatrix} = A \begin{pmatrix} f - 1/2 + \sqrt{f^2 - f + \beta^2 + 1/4} \\ \beta \end{pmatrix}. \tag{107}$$

Here A is the normalization constant and $\beta \neq 0$. For $f = 1/2$ we get

$$\begin{pmatrix} c_0^1 \\ c_{-1}^1 \end{pmatrix} = \frac{1}{\sqrt{2}} \begin{pmatrix} 1 \\ -1 \end{pmatrix}, \begin{pmatrix} c_0^2 \\ c_{-1}^2 \end{pmatrix} = \frac{1}{\sqrt{2}} \begin{pmatrix} 1 \\ 1 \end{pmatrix}. \tag{108}$$

From Eq. (108) one can see that for $f = 1/2$ the angular dependencies of the ground and first excited states wavefunctions are described by $\sin(\varphi/2)$ and $\cos(\varphi/2)$ respectively.

Fig. 21 shows the magnetic flux dependencies of the coefficients $|c_0|^2$, $|c_{-1}|^2$, and $|c_{+1}|^2$ for the electron ground, first and second excited states. From these plots one
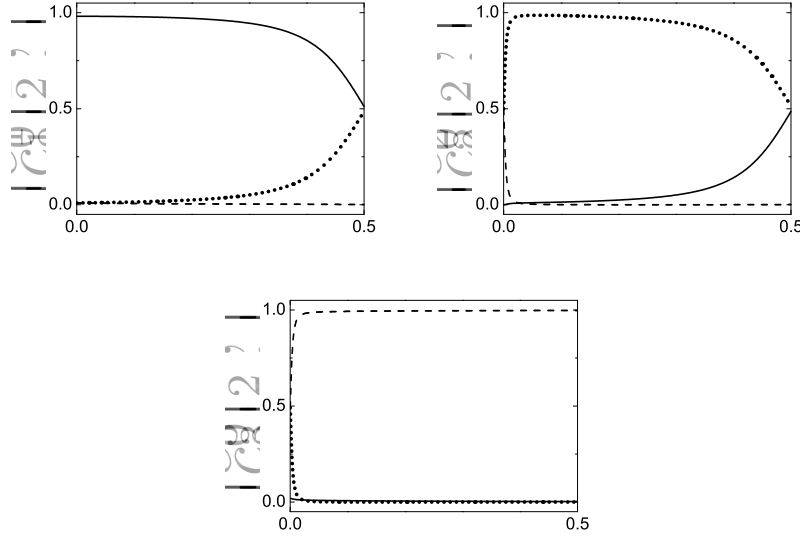
Fig. 21 Magnetic flux dependence of the wavefunction coefficients $|c_0|^2$ (solid line), $|c_{-1}|^2$ (dotted line), and $|c_{+1}|^2$ (dashed line): (a) for the ground state; (b) for the first excited state; (c) for the second excited state.

can see that the electron ground state is almost a pure $m = 0$ state in a wide region $0 \leq f \lesssim 1/4$. An admixture of the $m = -1$ wavefunction increases smoothly as one approaches the point of degeneracy $f = 1/2$. Finally, when $f = 1/2$, the ground state wavefunction is expressed as a difference of the $m = -1$ and $m = 0$ wavefunctions. The first and the second excited states behave differently. In a small region near

the point $f = 0$ the electron first and second excited states wavefunctions consist of a strong mixture of the $m = -1$ and $m = +1$ functions with a tiny admixture of the $m = 0$ function. In particular, when $f = 0$ the first and second excited states eigenfunctions with good accuracy can be expressed as the difference and the sum of the $m = -1$ and $m = +1$ functions respectively. Optical transitions between these states and the ground state are only allowed if the polarization of the associated optical excitations is either perpendicular (for the first excited state) or parallel (for the second excited state) to the direction of the applied in-plane electric field. Away from the $f = 0$ region, only the coefficient c_{-1} (in the case of the first excited state) or c_{+1} (in the case of the second excited state) remains in the Eq. (102), which now describes almost pure $m = +1$ and $m = -1$ states. When f exceeds $1/4$ the first excited state starts to contain a noticeable ad-mixture of $m = 0$ function, as discussed above, and for $f = 1/2$ the first excited state eigenfunction is expressed as a sum of the $m = -1$ and $m = 0$ wavefunctions in equal proportions, whereas the second excited state remains an almost pure $m = +1$ state.

The same trend in the evolution of wavefunctions of the three lowest energy states with changing the flux through the ring can be seen from perturbation theory. For $f = 0$, the degeneracy between the first and second excited states is removed in the second order in eER only. Nevertheless, as a result of the degeneracy, the introduction of any weak perturbation drastically modifies the wavefunctions corresponding to these states, turning them from the eigenstates of the angular momentum operator to the sine and cosine functions. With a slight increase of f, so that $f > \beta^2$, the first and the second excited states, which are not degenerate anymore for $f \neq 0$, become governed mainly by the diagonal terms of the Hamiltonian, which do not mix the $m = -1$ and $m = +1$ functions. When $f = 1/2$, the $m = -1$ and $m = 0$ states are degenerate in the absence of the electric field. This degeneracy is removed in the first order in eER. The off-diagonal matrix elements connecting $m = -1$ and $m = 0$ functions remain of the same order of magnitude as the difference between the diagonal terms of the Hamiltonian across a broad range of f values near $f = 1/2$. This results in strong mixing of the $m = -1$ and $m = 0$ components in the eigenfunctions of the ground and first excited states for $1/4 \lesssim f \leq 1/2$.

References

1. Y. Aharonov and D. Bohm. Significance of electromagnetic potentials in the quantum theory. *Phys. Rev.*, 115:485, 1959.
2. A.M. Alexeev and M.E. Portnoi. Terahertz transitions in Aharonov-Bohm quantum rings in an external electric field. *Phys. Stat. Sol. C*, 9:1309, 2012.
3. A.M. Alexeev and M.E. Portnoi. Electric dipole moment oscillations in Aharonov-Bohm quantum rings. *Phys. Rev. B*, 85:245419, 2012.
4. KL Koshelev, V Yu Kachorovskii, and M Titov. Resonant inverse faraday effect in nanorings. *Physical Review B*, 92(23):235426, 2015.
5. AM Alexeev, IA Shelykh, and ME Portnoi. Aharonov-bohm quantum rings in high-q microcavities. *Physical Review B*, 88(8):085429, 2013.

6. J.N. García, G. Medeiros-Ribeiro, K. Schmidt, T. Ngo, J.L. Feng, A. Lorke, J. Kotthaus, and P.M. Petroff. Intermixing and shape changes during the formation of InAs self-assembled quantum dots. *Appl. Phys. Lett.*, 71:2014, 1997.

7. J.M. García, T. Mankad, P.O. Holtz, P.J. Wellman, and P.M. Petroff. Electronic states tuning of InAs self-assembled quantum dots. *Appl. Phys. Lett.*, (24):3172, 1998.

8. A. Lorke, R.J. Luyken, M. Fricke, J.P. Kotthaus, G. Medeiros-Ribeiro, J.M. Garcia, and P.M. Petroff. Electronic structure of nanometer-size quantum dots and quantum rings. *Microelectronic engineering*, 47(1):95, 1999.

9. A. Lorke, L.R. Johannes, A.O. Govorov, J.P. Kotthaus, J.M. Garcia, and P.M. Petroff. Spectroscopy of nanoscopic semiconductor rings. *Phys. Rev. Lett.*, 84:2223, 2000.

10. E. Ribeiro, A.O. Govorov, W. Carvalho, and G. Medeiros-Ribeiro. Aharonov-Bohm signature for neutral polarized excitons in type-II quantum dot ensembles. *Phys. Rev. Lett.*, 92:126402, 2004.

11. T. Mano, T. Kuroda, S. Sanguinetti, T. Ochiai, T. Tateno, J. Kim, T. Noda, M. Kawabe, K. Sakoda, G. Kido, et al. Self-assembly of concentric quantum double rings. *Nano letters*, 5:425, 2005.

12. T. Kuroda, T. Mano, T. Ochiai, S. Sanguinetti, K. Sakoda, G. Kido, and N. Koguchi. Optical transitions in quantum ring complexes. *Phys. Rev. B*, 72:205301, 2005.

13. P. Offermans, P.M. Koenraad, J.H. Wolter, D. Granados, J.M. Garcia, V.M. Fomin, V.N. Gladilin, and J.T. Devreese. Atomic-scale structure of self-assembled In(Ga)As quantum rings in GaAs. *Appl. Phys. Lett.*, 87:131902, 2005.

14. M. Hanke, Y.I. Mazur, E. Marega Jr, Z.Y. AbuWaar, G.J. Salamo, P. Schäfer, and M. Schmidbauer. Shape transformation during overgrowth of InGaAs/GaAs (001) quantum rings. *Appl. Phys. Lett.*, 91:043103, 2007.

15. I.G. Kuskovsky, W. MacDonald, A.O. Govorov, L. Mourokh, X. Wei, M.C. Tamargo, M. Tadic, and F.M. Peeters. Optical Aharonov-Bohm effect in stacked type-II quantum dots. *Phys. Rev. B*, 76:035342, 2007.

16. C. Somaschini, S. Bietti, N. Koguchi, and S. Sanguinetti. Fabrication of multiple concentric nanoring structures. *Nano letters*, 9:3419, 2009.

17. J. Chen, W.S. Liao, X. Chen, T. Yang, S.E. Wark, D.H. Son, J.D. Batteas, and P.S. Cremer. Evaporation-induced assembly of quantum dots into nanorings. *ACS Nano*, 3:173, 2009.

18. M.D. Teodoro, V.L. Campo, V. Lopez-Richard, E. Marega, G.E. Marques, Y. Galv ao Gobato, F. Iikawa, M.J.S.P. Brasil, Z.Y. AbuWaar, V.G. Dorogan, Yu.I. Mazur, M. Benamara, and G.J. Salamo. Aharonov-Bohm interference in neutral excitons: effects of built-in electric fields. *Phys. Rev. Lett.*, 104:086401, 2010.

19. F. Ding, N. Akopian, B. Li, U. Perinetti, A. Govorov, F.M. Peeters, C.C. Bufon, C. Deneke, Y.H. Chen, A. Rastelli, et al. Gate controlled Aharonov-Bohm-type oscillations from single neutral excitons in quantum rings. *Phys. Rev. B*, 82:075309, 2010.

20. B. Roy, H. Ji, S. Dhomkar, F.J. Cadieu, L. Peng, R. Moug, M.C. Tamargo, and I.L Kuskovsky. Determination of excitonic size with sub-nanometer precision via excitonic Aharonov-Bohm effect in type-II quantum dots. *Appl. Phys. Lett.*, 100:213114, 2012.

21. Martin Elborg, Takeshi Noda, Takaaki Mano, Takashi Kuroda, Yuanzhao Yao, Yoshiki Sakuma, and Kazuaki Sakoda. Self-assembly of vertically aligned quantum ring-dot structure by multiple droplet epitaxy. *Journal of Crystal Growth*, 2017.

22. Yu D Sibirmovskii, IS Vasilevskii, AN Vinichenko, IS Eremin, NI Kargin, OS Kolentsova, and MN Strikhanov. Features of diffusion processes during drop epitaxy of quantum rings. *Bulletin of the Lebedev Physics Institute*, 41(9):243–246, 2014.

23. Yu D Sibirmovskii, IS Vasilevskii, AN Vinichenko, IS Eremin, DM Zhigunov, NI Kargin, OS Kolentsova, PA Martyuk, and MN Strikhanov. Photoluminescence of gaas/algaas quantum ring arrays. *Semiconductors*, 49(5):638–643, 2015.

24. Yu I Mazur, V Lopes-Oliveira, LD de Souza, V Lopez-Richard, MD Teodoro, VG Dorogan, M Benamara, J Wu, GG Tarasov, E Marega Jr, et al. Carrier transfer in vertically stacked quantum ring-quantum dot chains. *Journal of Applied Physics*, 117(15):154307, 2015.

25. Hee Dae Kim, Rin Okuyama, Kwangseuk Kyhm, Mikio Eto, Robert A Taylor, Aurelien L Nicolet, Marek Potemski, Gilles Nogues, Le Si Dang, Ku-Chul Je, et al. Observation of a biexciton wigner molecule by fractional optical aharonov-bohm oscillations in a single quantum ring. *Nano letters*, 16(1):27–33, 2015.

26. Heedae Kim, Woojin Lee, Seongho Park, Kwangseuk Kyhm, Koochul Je, Robert A Taylor, Gilles Nogues, Le Si Dang, and Jin Dong Song. Quasi-one-dimensional density of states in a single quantum ring. *Scientific reports*, 7, 2017.

27. HD Kim, Kwangseuk Kyhm, RA Taylor, AAL Nicolet, M Potemski, Gilles Nogues, KC Je, EH Lee, and JD Song. Excited exciton and biexciton localised states in a single quantum ring. *Applied Physics Letters*, 103(17):173106, 2013.

28. Vivaldo Lopes-Oliveira, Yuriy I Mazur, Leonardo Dias de Souza, Lucas A Bernardes Marçal, Jiang Wu, Marcio Daldin Teodoro, Angelo Malachias, Vitaliy G Dorogan, Mourad Benamara, Georgiy G Tarasov, et al. Structural and magnetic confinement of holes in the spin-polarized emission of coupled quantum ring–quantum dot chains. *Physical Review B*, 90(12):125315, 2014.

29. AM Beltrán, EA Marquis, AG Taboada, JM Ripalda, JM García, and SI Molina. Three dimensional atom probe imaging of gaassb quantum rings. *Ultramicroscopy*, 111(8):1073–1076, 2011.

30. Wei-Hsun Lin, Kai-Wei Wang, Yu-An Liao, Chun-Wei Pao, and Shih-Yen Lin. The formation mechanisms and optical characteristics of gasb quantum rings. *Journal of Applied Physics*, 114(5):053509, 2013.

31. Bidisha Roy, Haojie Ji, Siddharth Dhomkar, Maria C Tamargo, and Igor L Kuskovsky. Observation of oscillations in energy of aharonov–bohm excitons in type-ii znte/znse stacked submonolayer quantum dots. *physica status solidi (c)*, 11(7-8):1248–1251, 2014.

32. Haojie Ji, Siddharth Dhomkar, R Wu, V Shuvayev, V Deligiannakis, MC Tamargo, J Ludwig, Z Lu, D Smirnov, A Wang, et al. Optical anisotropy in type-ii znte/znse submonolayer quantum dots. *Journal of Applied Physics*, 119(22):224306, 2016.

33. M. Grochol, F. Grosse, and R. Zimmermann. Optical exciton Aharonov-Bohm effect, persistent current, and magnetization in semiconductor nanorings of type I and II. *Phys. Rev. B*, 74:115416, 2006.

34. A.G. Aronov and Yu.V. Sharvin. Magnetic flux effects in disordered conductors. *Rev. Mod. Phys.*, 59:755, 1987.

35. S. Viefers, P. Koskinen, P. Singha Deo, and M. Manninen. Quantum rings for beginners: energy spectra and persistent currents. *Physica E (Amsterdam)*, 21:1, 2004.

36. T. Ihn, A. Fuhrer, L. Meier, M. Sigrist, and K. Ensslin. Quantum physics in quantum rings. *Europhysics News*, 36:78, 2005.

37. I. Filikhin, S.G. Matinyan, and B. Vlahovic. Quantum mechanics of semiconductor quantum dots and rings. *ArXiv preprint arXiv:1206.1354*, 2012.

38. M Manninen, S Viefers, and SM Reimann. Quantum rings for beginners ii: Bosons versus fermions. *Physica E: Low-dimensional Systems and Nanostructures*, 46:119–132, 2012.

39. W. Ehrenberg and R.E. Siday. The refractive index in electron optics and the principles of dynamics. *Proc. Phys. Soc. London Sect. B*, 62:8, 1949.

40. H. Roy, B.and Ji, S. Dhomkar, F.J. Cadieu, L. Peng, R. Moug, M.C. Tamargo, and I.L. Kuskovsky. Distinguishability of stacks in ZnTe/ZnSe quantum dots via spectral analysis of Aharonov-Bohm oscillations. *The European Physical Journal B*, 86:1, 2013.

41. A.V. Chaplik. Magnetoexcitons in quantum rings and in antidots. *JETP*, 62:900, 1995.

42. A.V. Chaplik and A.O. Govorov. Multiply-charged magnetoexcitons in quantum-well systems. *Physica B: Condensed Matter*, 256:477, 1998.

43. R.A. Römer and M.E. Raikh. Aharonov-Bohm effect for an exciton. *Phys. Rev. B*, 62:7045, 2000.

44. T.V. Shahbazyan, I.E. Perakis, and M.E. Raikh. Spin correlations in nonlinear optical response: light-induced Kondo effect. *Phys. Rev. Lett.*, 84.

45. K. Maschke, T. Meier, P. Thomas, and S.W. Koch. Coherent dynamics of magnetoexcitons in semiconductor nanorings. *The European Physical Journal B-Condensed Matter and Complex Systems*, 19:599, 2001.

46. T. Meier, P. Thomas, and S.W. Koch. Linear and nonlinear optical properties of semiconductor nanorings with magnetic field and disorder-influence on excitons and biexcitons. *The European Physical Journal B-Condensed Matter and Complex Systems*, 22:249, 2001.

47. H. Hu, D.-J. Li, J.-L. Zhu, and J.-J. Xiong. Size effects on excitons in nano-rings. *Journal of Physics: Condensed Matter*, 12.

48. H. Hu, J.-L. Zhu, D.-J. Li, and J.-J. Xiong. Aharonov-Bohm effect of excitons in nanorings. *Phys. Rev. B*, 63:195307, 2001.

49. J. Song and S.E. Ulloa. Magnetic field effects on quantum ring excitons. *Phys. Rev. B*, 63:125302, 2001.

50. I. Galbraith, F.J. Braid, and R.J. Warburton. Magneto-excitons in semiconductor quantum rings. *Phys. Stat. Sol. A*, 190:781, 2002.

51. A.O. Govorov, A.V. Kalameitsev, R. Warburton, K. Karrai, and S.E. Ulloa. Excitons in quantum-ring structures in a magnetic field: optical properties and persistent currents. *Physica E: Low-dimensional Systems and Nanostructures*, 13:297, 2002.

52. L.G.G.V. Dias da Silva, S.E. Ulloa, and A.O. Govorov. Impurity effects on the Aharonov-Bohm optical signatures of neutral quantum-ring magnetoexcitons. *Phys. Rev. B*, 70:155318, 2004.

53. F. Palmero, J. Dorignac, J.C. Eilbeck, and R.A. Römer. Aharonov-Bohm effect for an exciton in a finite-width nanoring. *Phys. Rev. B*, 72:075343, 2005.

54. T.V. Bandos, A. Cantarero, and A. Garcia-Cristobal. Finite size effects on the optical transitions in quantum rings under a magnetic field. *The European Physical Journal B-Condensed Matter and Complex Systems*, 53:99, 2006.

55. Z. Barticevic, M. Pacheco, J. Simonin, and C.R. Proetto. Coulomb-interaction effects on the electronic structure of radially polarized excitons in nanorings. *Phys. Rev. B*, 73:165311, 2006.

56. Z. Dai and J.-L. Zhu. Dimensional effects on exciton states in nanorings. *Journal of Physics: Condensed Matter*, 19:346202, 2007.

57. E.N. Bogachek and U. Landman. Edge states, Aharonov-Bohm oscillations, and thermodynamic and spectral properties in a two-dimensional electron gas with an antidot. *Phys. Rev. B*, 52:14067, 1995.

58. W.C. Tan and J.C. Inkson. Electron states in a two-dimensional ring-an exactly soluble model. *Semiconductor Science and Technology*, 11:1635, 1996.

59. V.M. Kovalev and A.V. Chaplik. Aharonov-Bohm effect for plasmons in a finite-width quantum ring. *JETP letters*, 90:679, 2010.

60. C. González-Santander, F. Domínguez-Adame, and R.A. Römer. Excitonic Aharonov-Bohm effect in a two-dimensional quantum ring. *Phys. Rev. B*, 84:235103, 2011.

61. A.V. Maslov and D.S. Citrin. Enhancement of the Aharonov-Bohm effect of neutral excitons in semiconductor nanorings with an electric field. *Phys. Rev. B*, 67:121304, 2003.

62. A.M. Fischer, V.L. Campo, M.E. Portnoi, and R.A. Römer. Exciton storage in a nanoscale Aharonov-Bohm ring with electric field tuning. *Phys. Rev. Lett.*, 102:096405, 2009.

63. B. Li and F.M. Peeters. Tunable optical Aharonov-Bohm effect in a semiconductor quantum ring. *Phys. Rev. B*, 83:115448, 2011.

64. E. Yablonovitch. Inhibited spontaneous emission in solid-state physics and electronics. *Phys. Rev. Lett.*, 58:20592, 1987.

65. S. John. Strong localization of photons in certain disordered dielectric superlattices. *Phys. Rev. Lett.*, 58:2486, 1987.

66. E. Yablonovitch, T.J. Gmitter, and K.M. Leung. Photonic band structure: the face-centered-cubic case employing nonspherical atoms. *Phys. Rev. Lett.*, 67.

67. T.F. Krauss, R.M.D.L. Rue, and S. Brand. Two-dimensional photonic-bandgap structures operating at near-infrared wavelengths. *Nature*, 383:699, 1996.

68. S. Noda, A. Chutinan, and M. Imada. Trapping and emission of photons by a single defect in a photonic bandgap structure. *Nature*, 407:608, 2000.

69. Y. Takahashi, H. Hagino, Y. Tanaka, B.-S. Song, T. Asano, and S. Noda. High-Q nanocavity with a 2-ns photon lifetime. *Optics Express*, 15:17206, 2007.

70. Y. Tanaka, T. Asano, and S. Noda. Design of photonic crystal nanocavity with Q-factor of $\sim 10^9$. *Journal of Lightwave Technology*, 26:1532, 2008.

71. A.I. Nosich, E.I. Smotrova, S.V. Boriskina, T.M. Benson, and P. Sewell. Trends in microdisk laser research and linear optical modelling. *Optical and Quantum Electronics*, 39:1253, 2007.

72. E.M. Purcell. Spontaneous emission probabilities at radio frequencies. *Phys. Rev.*, 69:681, 1946.

73. J.-M. Gérard and B. Gayral. Strong Purcell effect for InAs quantum boxes in three-dimensional solid-state microcavities. *Journal of Lightwave Technology*, 17:2089, 1999.

74. G.S. Solomon, M. Pelton, and Y. Yamamoto. Single-mode spontaneous emission from a single quantum dot in a three-dimensional microcavity. *Phys. Rev. Lett.*, 86:3903, 2001.

75. A.J. Bennett, D.J.P. Ellis, A.J. Shields, P. Atkinson, I. Farrer, and D.A. Ritchie. Observation of the Purcell effect in high-index-contrast micropillars. *Appl. Phys. Lett.*, 90:191911, 2007.

76. A. Kiraz, P. Michler, C. Becher, B. Gayral, A. Imamoglu, L. Zhang, E. Hu, W.V. Schoenfeld, and P.M. Petroff. Cavity-quantum electrodynamics using a single InAs quantum dot in a microdisk structure. *Appl. Phys. Lett.*, 78:3932, 2001.

77. W.-H. Chang, W.-Y. Chen, H.-S. Chang, T.-P. Hsieh, J.-I. Chyi, and T.-M. Hsu. Efficient single-photon sources based on low-density quantum dots in photonic-crystal nanocavities. *Phys. Rev. Lett.*, 96:117401, 2006.

78. A. Badolato, K. Hennessy, M. Atatüre, J. Dreiser, E. Hu, P.M. Petroff, and A. Imamoğlu. Deterministic coupling of single quantum dots to single nanocavity modes. *Science*, 308:1158, 2005.

79. T. Yoshie, A. Scherer, J. Hendrickson, G. Khitrova, H. M. Gibbs, G. Rupper, C. Ell, O. B. Shchekin, and D. G. Deppe. Vacuum Rabi splitting with a single quantum dot in a photonic crystal nanocavity. *Nature (London)*, 432:200, 2004.

80. J.P. Reithmaier, G. Sek, A. Löffler, C. Hofmann, S. Kuhn, S. Reitzenstein, L.V. Keldysh, V.D. Kulakovskii, T.L. Reinecke, and A. Forchel. Strong coupling in a single quantum dotsemiconductor microcavity system. *Nature (London)*, 432:197, 2004.

81. E. Peter, P. Senellart, D. Martrou, A. Lemaitre, J. Hours, J.M. Gerard, , and J. Bloch. Exciton-photon strong-coupling regime for a single quantum dot embedded in a microcavity. *Phys. Rev. Lett.*, 95:067401, 2005.

82. K. Hennessy, A. Badolato, M. Winger, D. Gerace, M. Atatüre, S. Gulde, S. Fält, E.L. Hu, and A. Imamoğlu. Quantum nature of a strongly coupled single quantum dotcavity system. *Nature (London)*, 445:896, 2007.

83. M. Nomura, Y. Ota, N. Kumagai, S. Iwamoto, and Y. Arakawa. Large vacuum Rabi splitting in single self-assembled quantum dot-nanocavity system. *Applied Physics Express*, 1, 2008.

84. A. Laucht, N. Hauke, J.M. Villas-Bôas, F. Hofbauer, G. Böhm, M. Kaniber, and J.J. Finley. Dephasing of exciton polaritons in photoexcited InGaAs quantum dots in GaAs nanocavities. *Phys. Rev. Lett.*, 103:87405, 2009.

85. A. Laucht, F. Hofbauer, N. Hauke, J. Angele, S. Stobbe, M. Kaniber, G. Böhm, P. Lodahl, M.C. Amann, and J.J. Finley. Electrical control of spontaneous emission and strong coupling for a single quantum dot. *New Journal of Physics*, 11.

86. C. Kistner, K. Morgener, S. Reitzenstein, C. Schneider, S. Hofling, L. Worschech, A. Forchel, P. Yao, and S. Hughes. Strong coupling in a quantum dot micropillar system under electrical current injection. *Appl. Phys. Lett.*, 96:221102, 2010.

87. M. Lermer, N. Gregersen, F. Dunzer, S. Reitzenstein, S. Höfling, J. Mørk, L. Worschech, M. Kamp, and A. Forchel. Bloch-wave engineering of quantum dot micropillars for cavity quantum electrodynamics experiments. *Phys. Rev. Lett.*, 108:057402, 2012.

88. D.A.B. Miller, D.S. Chemla, T.C. Damen, A.C. Gossard, W. Wiegmann, T.H. Wood, and C.A. Burrus. Band-edge electroabsorption in quantum well structures: the quantum-confined Stark effect. *Phys. Rev. Lett.*, 53:2173, 1984.

89. C. Gerry and P. Knight. *Introductory Quantum Optics*. Cambridge University Press, 2005.

90. S. Haroche and J.M. Raimond. *Exploring the Quantum: atoms, Cavities, and Photons*. Oxford graduate texts in mathematics. OUP Oxford, 2006.

91. L. Mandel and E. Wolf. *Optical Coherence and Quantum Optics*. Cambridge University Press, 1995.
92. M.O. Scully and S. Zubairy. *Quantum Optics*. Cambridge University Press, 1997.
93. H.J. Carmichael. *Statistical Methods in Quantum Optics*. Number v. 1 in Statistical Methods in Quantum Optics. Springer, 1999.
94. H.J. Carmichael. *Statistical Methods in Quantum Optics 2: Non-Classical Fields*. Theoretical and Mathematical Physics. Springer, 2008.
95. L.D. Landau and E.M. Lifshitz. Quantum mechanics. *Course of Theoretical Physics*, 3:768, 1977.
96. A. Messiah. *Quantum Mechanics*, volume 2. North-Holland, Amsterdam, 1965.
97. H. Rigneault and S. Monneret. Field quantization and spontaneous emission in lossless dielectric multilayer structures. *Quantum and Semiclassical Optics: Journal of the European Optical Society Part B*, 9:1017, 1999.
98. G. Hétet, L. Slodička, A. Glätzle, M. Hennrich, and R. Blatt. QED with a spherical mirror. *Phys. Rev. A*, 82:063812, 2010.
99. M.A. Rippin and P.L. Knight. Modified spontaneous emission in cylindrical microcavities: waveguiding and distributed Bragg reflecting structures. *Journal of Modern Optics*, 43:807, 1996.
100. L.C. Andreani, G. Panzarini, and J.-M. Gérard. Strong-coupling regime for quantum boxes in pillar microcavities: theory. *Phys. Rev. B*, 60:13276, 1999.
101. I. Schuster, A. Kubanek, A. Fuhrmanek, T. Puppe, P.W.H. Pinkse, K. Murr, and G. Rempe. Nonlinear spectroscopy of photons bound to one atom. *Nature Physics*, 4:382, 2008.
102. F.P. Laussy, E. del Valle, and C. Tejedor. Strong coupling of quantum dots in microcavities. *Phys. Rev. Lett.*, 101:083601, 2008.
103. F. Bloch and A. Siegert. Magnetic resonance for nonrotating fields. *Phys. Rev.*, 57:522, 1940.
104. J. Von Neumann. Wahrscheinlichkeitstheoretischer Aufbau der Quantenmechanik. *Göttinger Nachrichten*, 1(10):245–272, 1927.
105. G. Lindblad. On the generators of quantum dynamical semigroups. *Communications in Mathematical Physics*, 48.
106. E.T. Jaynes and F.W. Cummings. Comparison of quantum and semiclassical radiation theories with application to the beam maser. *Proceedings of the IEEE*, 51:89, 1963.
107. T.R. Nielsen, P. Gartner, and F. Jahnke. Many-body theory of carrier capture and relaxation in semiconductor quantum-dot lasers. *Phys. Rev. B*, 69:235314, 2004.
108. N.S. Averkiev, M.M. Glazov, and A.N. Poddubnyi. Collective modes of quantum dot ensembles in microcavities. *JETP*, 108:836, 2009.
109. C.W. Gardiner and P. Zoller. *Quantum noise: a handbook of Markovian and non-Markovian quantum stochastic methods with applications to quantum optics*, volume 56. Springer, 2004.
110. Z. Barticevi, G. Fuster, and M. Pacheco. Effect of an electric field on the Bohm-Aharonov oscillations in the electronic spectrum of a quantum ring. *Phys. Rev. B*, 65:193307, 2002.
111. A. Bruno-Alfonso and A. Latgé. Aharonov-Bohm oscillations in a quantum ring: eccentricity and electric-field effects. *Phys. Rev. B*, 71:125312, 2005.
112. O.V. Kibis, S.V. Malevannyy, L. Huggett, D.G.W. Parfitt, and M.E. Portnoi. Superlattice properties of helical nanostructures in a transverse electric field. *Electromagnetics*, 25:425, 2005.
113. O.V. Kibis and M.E. Portnoi. Semiconductor nanohelix in electric field: a superlattice of the new type. *Tech. Phys. Lett.*, 33:878, 2007.
114. O.V. Kibis and M.E. Portnoi. Superlattice properties of semiconductor nanohelices in a transverse electric field. *Physica E (Amsterdam)*, 40:1899, 2008.
115. M.E. Portnoi, O.V. Kibis, V.L. Campo Jr., M. Rosenau da Costa, L. Huggett, and S.V. Malevannyy. Helical nanostructures and Aharonov-Bohm quantum rings in a transverse electric field. *Proc. 28th ICPS, AIP Conference Proceedings*, 893:703, 2007.
116. E.A. Avrutin and M.E. Portnoi. Estimate of the lifetimes of nonequilibrium carriers in a semiconductor irradiated with heavy ions. *Sov. Phys. Semicond.*, 22:968, 1988.
117. M.E. Portnoi, O.V. Kibis, and M. Rosenau da Costa. Terahertz applications of carbon nanotubes. *Superlatt. Microstruct.*, 43:399, 2008.

118. M.E. Portnoi, M. Rosenau da Costa, O.V. Kibis, and I.A. Shelykh. Magnetically controlled terahertz absorption and emission in carbon nanotubes. *Int. J. Mod. Phys. B*, 23:2846, 2009.
119. K.G. Batrakov, O.V. Kibis, P.P. Kuzhir, M. Rosenau da Costa, and M.E. Portnoi. Terahertz processes in carbon nanotubes. *J. Nanophoton.*, 4:041665, 2010.
120. R.R. Hartmann, I.A. Shelykh, and M.E. Portnoi. Excitons in narrow-gap carbon nanotubes. *Phys. Rev. B*, 84:035437, 2011.
121. K.V. Kavokin, M.A. Kaliteevski, R.A. Abram, A.V. Kavokin, S. Sharkova, and I.A. Shelykh. Stimulated emission of terahertz radiation by exciton-polariton lasers. *Appl. Phys. Lett.*, 97:201111, 2010.
122. E. del Valle and A. Kavokin. Terahertz lasing in a polariton system: quantum theory. *Phys. Rev. B*, 83:193303, 2011.
123. I.G. Savenko, I.A. Shelykh, and M.A. Kaliteevski. Nonlinear terahertz emission in semiconductor microcavities. *Phys. Rev. Lett.*, 107:027401, 2011.
124. C. Weisbuch, M. Nishioka, A. Ishikawa, and Y. Arakawa. Observation of the coupled exciton-photon mode splitting in a semiconductor quantum microcavity. *Phys. Rev. Lett.*, 69:3314, 1992.
125. See, e.g., a special volume devoted to the physics of microcavities. *Phys. Stat. Sol. B*, 242(11), 2005.
126. J. Kasprzak, M. Richard, S. Kundermann, A. Baas, P. Jeambrun, J.M.J. Keeling, F.M. Marchetti, M.H. Szymanska, R. André, J.L. Staehli, V. Savona, P.B. Littlewood, B. Deveaud, and Le Si Dang. Boseeinstein condensation of exciton polaritons. *Nature (London)*, 443:409, 2006.
127. R. Balili, V. Hartwell, D. Snoke, L. Pfeiffer, and K. West. Bose-einstein condensation of microcavity polaritons in a trap. *Scince*, 316:1007, 2007.
128. A. Amo, D. Sanvitto, F.P. Laussy, D. Ballarini, E. del Valle, A. Lemaître M.D. Martin, J. Bloch, D.N. Krizhanovskii, M.S. Skolnick, C. Tejedor, and L. Vina. Collective fluid dynamics of a polariton condensate in a semiconductor microcavity. *Nature (London)*, 457:291, 2009.
129. T.C.H. Liew, I.A. Shelykh, and G. Malpuech. Polaritonic devices. *Physica E*, 43:1543, 2011.
130. S. Christopoulos, G. Baldassarri Höger von Högersthal, A.J.D. Grundy, P.G. Lagoudakis, A.V. Kavokin, J.J. Baumberg, G. Christmann, R. Butté, E. Feltin, J.-F. Carlin, and N. Grandjean. Room-temperature polariton lasing in semiconductor microcavities. *Phys. Rev. Lett.*, 98:126405, 2007.
131. C. Leyder, T.C.H. Liew, A.V. Kavokin, I.A. Shelykh, M. Romanelli, J.Ph. Karr, E. Giacobino, and A. Bramati. Interference of coherent polariton beams in microcavities: polarization-controlled optical gates. *Phys. Rev. Lett.*, 99:196402, 2007.
132. A.V. Kavokin, I.A. Shelykh, T. Taylor, and M.M. Glazov. Vertical cavity surface emitting terahertz laser. *Phys. Rev. Lett.*, 108:197401, 2012.
133. C. Ciuti. Branch-entangled polariton pairs in planar microcavities and photonic wires. *Phys. Rev. B*, 69:245304, 2004.
134. S. Savasta, O.Di Stefano, V. Savona, and W. Langbein. Quantum complementary of microcavity polaritons. *Phys. Rev. Lett.*, 94:246401, 2005.
135. R. Johne, N.A. Gippius, G. Pavlovic, D.D. Solnyshkov, I.A. Shelykh, and G. Malpuech. Entangled photon pairs produced by a quantum dot strongly coupled to a microcavity. *Phys. Rev. Lett.*, 100:240404, 2008.
136. M.A. Kaliteevski, S. Brand, R.A. Abram, A. Kavokin, and Le Si Dang. Whispering gallery polaritons in cylindrical cavities. *Phys. Rev. B*, 75:233309, 2007.
137. F.P. Laussy, E. del Valle, and C. Tejedor. Luminescence spectra of quantum dots in microcavities. I. Bosons. *Phys. Rev. B*, 79:235325, 2009.
138. E. del Valle, F.P. Laussy, and C. Tejedor. Luminescence spectra of quantum dots in microcavities. II. Fermions. *Phys. Rev. B*, 79:235326, 2009.
139. E. del Valle and F.P. Laussy. Mollow triplet under incoherent pumping. *Phys. Rev. Lett.*, 105:233601, 2010.
140. I.G. Savenko, O.V. Kibis, and I.A. Shelykh. Asymmetric quantum dot in a microcavity as a nonlinear optical element. *Phys. Rev. A*, 85:053818, 2012.

141. P.A. George, C. Manolatou, F. Rana, A.L. Bingham, and D.R. Grischkowsky. Integrated waveguide-coupled terahertz microcavity resonators. *Appl. Phys. Lett.*, 91:191122, 2007.

142. C.M. Yee and M.S. Sherwin. High-Q terahertz microcavities in silicon photonic crystal slabs. *Appl. Phys. Lett.*, 94:154104, 2009.

143. Y. Todorov, A.M. Andrews, I. Sagnes, R. Colombelli, P. Klang, G. Strasser, and C. Sirtori. Strong light-matter coupling in subwavelength metal-dielectric microcavities at terahertz frequencies. *Phys. Rev. Lett.*, 102:186402, 2009.

144. S. Sree Harsha, N. Laman, and D. Grischkowsky. High-Q terahertz Bragg resonances within a metal parallel plate waveguide. *Appl. Phys. Lett.*, 94:091118, 2009.

145. O.V. Kibis, D.G.W. Parfitt, and M.E. Portnoi. Superlattice properties of carbon nanotubes in a transverse electric field. *Phys. Rev. B*, 71:035411, 2005.

146. E.T. Jaynes and F.W. Cummings. Comparison of quantum and semiclassical radiation theories with application to the beam maser. *Proc. IEEE*, 51:89, 1963.

147. M.O. Scully and M.S. Zubairy. *Quantum Optics*. University Press, Cambridge, 2001.

148. C. Cohen-Tannoudji, J. Dupont-Roc, and G. Grynberg. *Atom-Photon Interactions: basic Processes and Applications*. Wiley, Chichester, 1998.

149. C.A. Vera, H. Vinck-Posada, and A. González. Polariton lasing in a multilevel quantum dot strongly coupled to a single photon mode. *Phys. Rev. B*, 80:125302, Sep 2009.

150. B.S. Williams. Terahertz quantum-cascade lasers. *Nature Photonics*, 1:517, 2007.

151. M.A. Belkin, J.A. Fan, S. Hormoz, F. Capasso, S.P. Khanna, M. Lachab, A.G. Davies, E.H. Linfield, et al. Terahertz quantum cascade lasers with copper metal-metal waveguides operating up to 178 K. *Optics Express*, 16:3242, 2008.

152. S. Kumar, Q. Hu, and J.L. Reno. 186 K operation of terahertz quantum-cascade lasers based on a diagonal design. *Appl. Phys. Lett.*, 94.

153. G.L. Carr, M.C. Martin, W.R. McKinney, K. Jordan, G.R. Neil, and G.P. Williams. High-power terahertz radiation from relativistic electrons. *Nature*, 420.

154. M. Tonouchi. Cutting-edge terahertz technology. *Nature Photonics*, 1:97, 2007.

155. D.L. Woolard, T.R. Globus, B.L. Gelmont, M. Bykhovskaia, A.C. Samuels, D. Cookmeyer, J.L. Hesler, T.W. Crowe, J.O. Jensen, J.L. Jensen, et al. Submillimeter-wave phonon modes in DNA macromolecules. *Phys. Rev. E*, 65:051903, 2002.

156. T.R. Globus, D.L. Woolard, T. Khromova, T.W. Crowe, M. Bykhovskaia, B.L. Gelmont, J. Hesler, and A.C. Samuels. THz-spectroscopy of biological molecules. *Journal of Biological Physics*, 29:89, 2003.

157. P.F. Taday, I.V. Bradley, D.D. Arnone, and M. Pepper. Using terahertz pulse spectroscopy to study the crystalline structure of a drug: a case study of the polymorphs of ranitidine hydrochloride. *Journal of pharmaceutical sciences*, 92:831, 2003.

158. C. Jansen, F. Neubauer, J. Helbig, D.M. Mittleman, and M. Koch. Flexible Bragg reflectors for the terahertz regime composed of polymeric compounds. In *Infrared and Millimeter Waves, 2007 and the 2007 15th International Conference on Terahertz Electronics. IRMMW-THz. Joint 32nd International Conference*, page 984. IEEE, 2007.

159. M. Lax. Formal theory of quantum fluctuations from a driven state. *Phys. Rev.*, 129:2342, 1963.

160. N. Wiener. Generalized harmonic analysis. *Acta Mathematica*, 55:117, 1930.

161. A. Khintchine. Korrelationstheorie der stationären stochastischen prozesse. *Mathematische Annalen*, 109:604, 1934.